Two phase flow simulation of conjugate natural convection of the nanofluid in a partitioned heat exchanger containing several conducting obstacles

Garoosi, Faroogh; Rashidi, Mohammad Mehdi

DOI:
10.1016/j.ijmecsci.2017.06.020

Document Version
Peer reviewed version

Citation for published version (Harvard):
Garoosi, F & Rashidi, MM 2017, 'Two phase flow simulation of conjugate natural convection of the nanofluid in a partitioned heat exchanger containing several conducting obstacles', *International Journal of Mechanical Sciences*, vol. 130, pp. 282-306. https://doi.org/10.1016/j.ijmecsci.2017.06.020

Two phase flow simulation of conjugate natural convection of the nanofluid in a partitioned heat exchanger containing several conducting obstacles

Faroogh Garoosi , Mohammad Mehdi Rashidi

PII: S0020-7403(17)30937-2
DOI: 10.1016/j.ijmecsci.2017.06.020
Reference: MS 3748

To appear in: *International Journal of Mechanical Sciences*

Received date: 12 April 2017
Revised date: 30 May 2017
Accepted date: 14 June 2017

Please cite this article as: Faroogh Garoosi , Mohammad Mehdi Rashidi , Two phase flow simulation of conjugate natural convection of the nanofluid in a partitioned heat exchanger containing several conducting obstacles , *International Journal of Mechanical Sciences* (2017), doi: 10.1016/j.ijmecsci.2017.06.020

Highlight

- By increasing the thermal conductivity ratio (K_r), the heat transfer rate enhances.
- At high *Ra*, type and size of the nanoparticles have a minor impact on the $\overline{Nu}_{tot}$.
- At high *Ra*, orientation of the conductive partition has a significant impact on the $\overline{Nu}_{tot}$.
- At low *Ra*, by dividing the conductive obstacle into the small parts, the $\overline{Nu}_{tot}$ decreases.
- At low Ra, distribution of Al_2O_3 and TiO_2 nanoparticles is fairly non-uniform.

Two phase flow simulation of conjugate natural convection of the nanofluid in a partitioned heat exchanger containing several conducting obstacles

Faroogh Garoosi[a,*], Mohammad Mehdi Rashidi[b]

[a]Department of Mechanical Engineering, University of Semnan , Semnan, Iran

[a]Department of Mechanical Engineering, Aliabad Katoul Branch, Islamic Azad University, Aliabad Katoul, Iran

[b]Department of Civil Engineering, School of Engineering, University of Birmingham, Birmingham, the UK

Corresponding author: faroogh.garoosi@semnan.ac.ir, Garoosi.faroogh@yahoo.com, Tel:+989112748341

Abstract

In this paper, numerical results for conjugate natural convection flow and heat transfer in a heat exchanger divided by a partition with finite thickness and thermal conductivity are presented using Boungiorno's two phase model. A series of numerical simulation is carried out using the finite volume method over a wide range of the Rayleigh number ($10^4 \le Ra \le 10^7$), volume fraction ($0 \le \varphi \le 0.05$), diameter ($25nm \le d_p \le 145nm$) and type of the nanoparticles (*Cu*, Al_2O_3 and TiO_2). In addition, the effects of three types of influential factors such as: thermal conductivity ratio ($0.1 \le K_r \le 25$), orientation of conductive partition and segmentation of the conductive obstacle on fluid flow and heat transfer characteristics are investigated. Results show that at low *Ra*, by dividing the conductive obstacle into the nine small segments, the heat transfer rate and absolute values of stream function decrease significantly. It is also observed that by increasing the *Ra* and thermal conductivity ratio (K_r) the heat transfer rate increase. Moreover, it is found that by changing the orientation of the conductive partition from vertical to horizontal

mode, the heat transfer rate alters significantly. Finally, the results demonstrate that the effect of the thermophoresis force for solid particles with high thermal conductivity (like *Cu*) is negligible.

Keywords: *Conjugate natural convection, Nanofluid, Numerical simulation, Two phase model, conductive obstacles, Conductive partition*

Nomenclature

A	surface area per unit depth $A = 2(L_1 + L_2)$ and/or $A = W$, m
C_p	specific heat, $J\ kg^{-1}\ K^{-1}$
D_B	Brownian coefficient, $kg\ m^{-1}\ s^{-1}$
d_f	diameter of the base fluid molecule, m
d_p	diameter of the nanoparticle, m
D_T	Thermophoresis coefficient, $kg\ m^{-1}\ s^{-1}\ K^{-1}$
g	Gravitational acceleration, ms^{-2}
H	enclosure height, m
J_p	Particle flux vector, $kg\ m^{-2}\ s^{-1}$
k	thermal conductivity, $Wm^{-1}K^{-1}$
k_b	Boltzmann's constant=$1.38066\times10^{-23}\ JK^{-1}$
K_r	Thermal conductivity ratio of solid wall to pure fluid
L	Length of the heater, cooler and conductive wall
$\overline{Nu}_i$	Average Nusselt number on the walls of the each heater or cooler
$\overline{Nu}_{tot}$	Sum of $\overline{Nu}_i$ of all heaters or coolers
p	pressure, Nm^{-2}

P	dimensionless pressure
Pr_f	Prandtl number ($=\nu_f/\alpha_f$)
Ra_f	Rayleigh number ($=g\beta_f(T_h-T_c)H^3/\alpha_f\nu_f$)
Re_B	Brownian-motion Reynolds number
T	temperature, K
T_{fr}	freezing point of the base fluid, K
u,v	velocity components, ms^{-1}
u_B	Brownian velocity of the nanoparticle, ms^{-1}
U, V	dimensionless velocity components
W	Length of the hot and cold surfaces
x,y	Cartesian coordinates, m
X, Y	dimensionless Cartesian coordinates

Greek symbols

α	thermal diffusivity, m^2s^{-1}
β	Thermal expansion coefficient, K^{-1}
γ	solid-to-fluid volume ratio
θ	dimensionless temperature
μ	dynamic viscosity, kg m^{-1} s^{-1}
ν	kinematic viscosity, m^2s^{-1}
ρ	density, kg m^{-3}
φ	volume fraction of the nanoparticles (vol. nanoparticles / total vol.)
ψ	stream function($=-\int_{Y_0}^{Y}U\partial Y+\psi(X,Y_0)$)

Subscripts

c	cold wall
f	fluid
h	hot wall
nf	nanofluid
p	solid nanoparticles
s	Solid wall (conductive wall)

1. Introduction

Buoyancy driven natural convection in a square enclosure is a classical problem of fundamental fluid mechanics and heat transfer as this phenomenon is very common in several engineering and environmental problems such as nuclear reactors, double pane windows, cooling electrical components, solar collectors and heat exchangers [1]. In the last decade, many researchers have simulated the heat removal mechanism by means of natural convection in a heat exchanger containing several hot and cold pipes. Dai et al. [2], Garoosi et al. [3], Gap et al. [4] and Wang et al. [5] studied free convection heat transfer between hot and cold micro-tubes in a heat exchanger. Their results indicated that, the maximum heat transfer performance can be achieved when the hot tubes are located lower than the cold ones. Similar observation was reported by Qi-Hong Deng [6] who investigated natural convection heat transfer in a two-dimensional square enclosure with two and three discrete heat source–sink pairs on the vertical sidewalls. He found that, heat transfer relationship between hot and cold surfaces in terms of the average Nusselt number values, is one to one in a reversed manner such that the amount of heat released by the top and bottom sources is equally absorbed by the bottom and top sinks on the opposite sidewall.

Conjugate natural convection heat transfer in enclosures inserted with solid obstacles has received considerable attention because of its importance to many engineering systems, such as: furnace design, thermal storage systems and home ventilation. More precisely, in the design and construction of buildings, the thermo-physical properties of the finite thickness and conductive partition significantly affect the thermal insulation and indoor air circulation performances. From an academic perspective, this issue not only enriches our understandings on the flow physics and heat transfer characteristics in more complex configurations but also provides a suitable framework for the cross validation between the results obtained by different numerical methods and experimental techniques. The works of Oztop et al. [7], Das et al. [8], Raji et al. [9], Hu et al. [10], Ren et al. [11] and Khatamifar et al. [12] are just a few examples of such studies in which they numerically investigated conjugate natural convection in square enclosure. Their results indicated that size, number, position and physical properties of the solid obstacles have deep influences on the enclosed fluid flow and heat transfer structures.

However, low thermal conductivity of traditional heat transfer fluids such as water, oil, and ethylene glycol mixture is an important limitation in improving the performance and compactness of heat exchangers. One way to overcome this disadvantage is by adding solid nanoparticles with high thermal conductivity into the working fluid. However, the dispersion of a small amount of solid nanoparticles in traditional working fluid can significantly change their thermo-physical properties. As a result, in the last decade, different aspects of nanofluids have been studied comprehensively [13]. Generally, numerical simulation of the fluid flow, the temperature distribution and heat transfer characteristics of the nanofluid can be performed by using two different methods; single-phase (homogenous) and two phase models. In the homogenous method, it is assumed that the solid particles and the base fluid are in thermal

equilibrium and have the same temperature and velocity. Selimefendigil et al. [14–17], Sheikholeslami et al. [18–20] and Kefayati [21–24] numerically simulated the effects of magnetic field on natural, mixed and forced convection of nanofluid in different geometries using the single-phase model. Their results showed that the presence of the magnetic field retarded the velocity field and convection within the enclosure. In addition, they found that by increasing the Rayleigh number and volume fraction of the nanoparticles, the average Nusselt number enhances. In a similar work, Bouchoucha et al. [25], Sheremet et al. [26], Job et al. [27], Rashad et al. [28], Purusothaman et al. [29] and Cho et al. [30] presented a numerical simulation of natural and mixed convection heat transfer of nanofluids in square and rectangular enclosures. They used Maxwell–Garnett [31] and Brinkman models [32] to determine effective thermal conductivity and dynamic viscosity of the nanofluid. They found that, there is a direct correlation between nanoparticles concentration and total Nusselt number such that by increasing the volume fraction of solid particles the heat transfer rate enhances. However, Corcione [33] proposed two new empirical correlations for predicting the effective thermal conductivity and dynamic viscosity of nanofluids, based on a wide variety of experimental data reported in the literature. He found that, the traditional theories like Maxwell–Garnett [31] and Brinkman models [32] fail abundantly when employed for nanofluids. Furthermore, his proposed models show reasonably good agreement with the experimental results and give better predictions for the effective thermal conductivity and dynamic viscosity of nanofluids compared to existing classical models. Wang et al. [34] conducted a numerical simulation to investigate the problem of forced convection of nanofluid in an open enclosures using Corcione's model [33]. Their results show that the average Nusselt number enhances with increasing the nanoparticle volume fraction up to an optimal particle loading where maximum heat transfer rate occurs. Furthermore,

they found that by decreasing the nanoparticles diameter and increasing the average temperature of the nanofluid, the optimal particle loading and heat transfer rate increase. However, experimental studies by Wen et al. [35] question the validity of the homogeneous model for simulation of the nanofluids. Their results indicate that slip velocity between the base fluid and particles may not be zero due to several factors such as Brownian and gravity forces; therefore it seems that the two phase approach is better model to apply the nanofluid. In a pioneering work, Buongiorno [36] developed a non-homogeneous equilibrium model by considering the effects of the Brownian diffusion and thermophoresis force as two important primary slip mechanisms between fluid and solid phases. His results indicate that due to Brownian diffusion and thermophoresis force, solid particles migrate from hot to the cold regions. In addition, he found that, the effects of the thermophoresis force for solid particles with high thermal conductivity (i.e. copper) are negligible. Similar observation was reported by Sheremet et al. [37], Esfandiary et al. [38], Motlagh et al. [39], Koriko et al. [40], Malvandi et al. [41–43] and Hedayati et al. [44–46] who investigated natural, mixed and forced convection heat transfer of nanofluids in an open and closed enclosures using Buongiorno's model [36]. Pakravan et al. [47], Sheikhzadeh et al. [48] and Corcione et al. [49] conducted a comparison study between single phase model and Buongiorno's two phase model, showing that the transport model guarantees a better agreement with experimental results.

Based on the above literature survey and to the best of authors' knowledge, conjugate natural convection of nanofluid in a square enclosure containing a conductive partition and several disconnected conducting solid blocks has never been studied in the literature despite its importance in many engineering systems such as heat exchangers. In the physical configuration under consideration here, the heat exchange process between several differentially heated

cylinders enclosed in an adiabatic enclosure may involve the interaction of buoyant streams individually induced by heating or cooling around them. Such natural convection configuration is primarily of fundamental relevance to the heat tracing system commonly used to minimize heat exchange of a piping system with the ambient in order to prevent the fluids contained in the pipelines from freezing or condensing. The main objective of the current investigation is to analyze the effects of the Rayleigh number ($10^4 \le Ra \le 10^7$), volume fraction ($0 \le \varphi \le 0.05$), diameter ($25nm \le d_p \le 145nm$) and type of the nanoparticles (*Cu*, Al_2O_3 and TiO_2) on the fluid flow and heat transfer characteristics of the nanofluids. In addition, the effects of three types of influential factors such as: thermal conductivity ratio ($0.1 \le K_r \le 25$), orientation of conductive partition and segmentation of the conductive obstacle on the heat transfer performance of the heat exchanger are investigated.

2. Problem Statement

The problem considered in the present study is conjugate natural convection–conduction in a square enclosure containing a conductive partition and several disconnected conducting solid blocks (see Fig. 1). Hot and cold surfaces are maintained at the constant but different temperature ($T_h = 315K \ge T_c = 305K$) while other parts of the enclosure walls are all thermally insulated. The nanofluid in the enclosure is treated as a Newtonian and incompressible fluid. With the Boussinesq approximation, the thermo-physical properties of the working fluid are assumed to be constant except for variation in density of the buoyancy terms in the momentum equations (see Table 1 [50]).

3. Mathematical Formulation

The governing equations (mass, momentum and energy volume fraction conservation) for a steady, laminar and incompressible flow are as follows [26,36]:

$$\nabla \cdot \vec{V} = 0, \tag{1}$$

$$\rho_{nf} \vec{V}.\nabla\vec{V} = -\nabla P + \nabla.\mu_{nf}\nabla\vec{V} + (\rho\beta)_{nf}(T - T_c)g \tag{2}$$

$$(\rho C_p)_{nf} \vec{V}.\nabla T = \nabla.k_{nf}\nabla T - C_{p.p}\vec{J}_p.\nabla T \tag{3}$$

$$\vec{V}.\nabla\varphi = -\frac{1}{\rho_p}\nabla \cdot \overrightarrow{J_p}, \tag{4}$$

$$\overrightarrow{J_p} = \vec{J}_{p,B} + \vec{J}_{p,T}, \tag{5}$$

Heat conduction equation for the temperature in conductive walls and obstacles is given as:

$$\frac{\partial^2 T}{\partial x^2} + \frac{\partial^2 T}{\partial y^2} = 0 \tag{6}$$

The first and second term in Eq. (5) are the drift flux owing to the Brownian motion based on the model of Einstein-Stokes's [36] and thermophoretic effects [51] which are calculated as:

$$\vec{J}_{p,B} = -\rho_p D_B \nabla\varphi, \qquad where \;\; D_B = \frac{k_B T}{3\pi\mu_f d_p}. \tag{7}$$

$$\vec{J}_{p,T} = -\rho_p D_T \nabla T, \qquad where \;\; D_T = 0.26\frac{k_f}{2k_f + k_p}\frac{\mu_f}{\rho_f T}\varphi, \tag{8}$$

The thermo-physical properties of the nanofluid can be determined as follows [13]:

$$\rho_{nf} = (1-\varphi)\rho_f + \varphi\rho_p, \tag{9}$$

$$(\rho C_p)_{nf} = (1-\varphi)(\rho C_p)_f + \varphi(\rho C_p)_p, \tag{10}$$

$$(\rho\beta)_{nf} = (1-\varphi)(\rho\beta)_f + \varphi(\rho\beta)_p, \tag{11}$$

The effective thermal conductivity and dynamic viscosity of the nanofluid can be approximated by the model of Corcione [33] as:

$$\mu_{nf} = \mu_f \big/ (1 - 34.87(d_p / d_f)^{-0.3} \varphi^{1.03}), \tag{12}$$

$$\frac{k_{nf}}{k_f} = 1 + 4.4\,\mathrm{Re}_B^{0.4}\,\mathrm{Pr}^{0.66}\left(\frac{T}{T_{fr}}\right)^{10}\left(\frac{k_p}{k_f}\right)^{0.03}\varphi^{0.66}, \tag{13}$$

$$\mathrm{Re}_B = \frac{\rho_f u_B d_p}{\mu_f}, \tag{14}$$

$$u_B = \frac{2k_b T}{\pi \mu_f {d_p}^2}. \tag{15}$$

In order to proceed to the numerical solution of the system, the following non dimensional variables are defined based on the pure fluid properties:

$$X = \frac{x}{H}, \quad Y = \frac{y}{H}, \quad U = \frac{u\,H}{\alpha_f}, \quad V = \frac{vH}{\alpha_f}, \quad P = \frac{pH^2}{\rho_{nf}\alpha_f^2},$$
$$\theta = \frac{T - T_c}{T_h - T_c}, \quad Ra = \frac{g\beta_f (T_h - T_c) H^3}{\alpha_f \nu_f}, \ \mathrm{Pr}_f = \frac{\nu_f}{\alpha_f}, \quad K_r = \frac{k_s}{k_f}, \tag{16}$$

By considering no slip condition and zero flux of nanoparticles ($\vec{J}_p \cdot n = 0$) at the walls, the boundary conditions would be adjusted as follows [47,48]:

$$u = v = 0, \frac{\partial \varphi}{\partial n} = 0, \frac{\partial T}{\partial n} = 0 \quad \text{on the insulated walls of the enclosure}$$
$$u = v = 0, \frac{\partial \varphi}{\partial n} = -\frac{D_T}{D_B}\frac{\partial T}{\partial n}, T = T_h \quad \text{on the hot surfaces} \tag{17}$$
$$u = v = 0, \frac{\partial \varphi}{\partial n} = -\frac{D_T}{D_B}\frac{\partial T}{\partial n}, T = T_c \quad \text{on the cold surfaces}$$
$$u = v = 0, \frac{\partial \varphi}{\partial n} = -\frac{D_T}{D_B}\frac{\partial T}{\partial n}, \quad k_s\left(\frac{\partial T}{\partial n}\right)_s = k_{nf}\left(\frac{\partial T}{\partial n}\right)_{nf} \quad \text{on walls of the conductive surface}$$

The average Nusselt number for each hot and cold surface inside enclosure or on the walls of the enclosure is computed as:

$$\overline{Nu}_i = \frac{\int_{X_h-\frac{L}{2}}^{X_h+\frac{L}{2}} \frac{k_{nf}(\varphi)}{k_f}\left\{\left.\frac{\partial\theta}{\partial Y}\right|_{bottom} + \left.\frac{\partial\theta}{\partial Y}\right|_{upper}\right\}dX + \int_{Y_h-\frac{L}{2}}^{Y_h+\frac{L}{2}} \frac{k_{nf}(\varphi)}{k_f}\left\{\left.\frac{\partial\theta}{\partial X}\right|_{left} + \left.\frac{\partial\theta}{\partial X}\right|_{right}\right\}dY}{A} \quad (18)$$

4. Numerical implementation, grid study and verification

In the present computation, the finite volume method is applied for discretization of governing equations and boundary conditions, with the SIMPLE algorithm [52] to couple the pressure-velocity system. In order to solve the convection and diffusion terms, second order QUICK and central difference schemes are utilized, respectively. The TDMA (Tri-Diagonal Matrix Algorithm) method [52] is applied on equation systems until the normalized residuals of the momentum, energy and volume fraction equations became less than 10^{-6}, 10^{-6} and 10^{-7}, respectively. The above convergence criterion assures an acceptable solution.

In order to determine a proper grid size for the study, a grid independency test is conducted for cases 1A, 2D and 3D at two extreme Rayleigh number (Ra = 10^4 and 10^7). Seven different uniform grids are chosen and total Nusselt number is used as a sensitivity measure of the accuracy of the solution. Table 2 reveals that the grid independence is achieved when the grid size is up to 149×149 points so that the values of total Nusselt number don't alter significantly with the improvement of finer grid. Thus, by considering both accuracy and the computational time, the grid system of 149×149 points is chosen for all simulation reported in this study.

The numerical code was validated against the results obtained by Das et al. [8] who have investigated conjugate natural convection heat transfer in an inclined square enclosure containing

a conductive obstacle (see Fig. 2). Additional validation of the numerical code was conducted successfully against the numerical results obtained by Sheikhzadeh et al. [48] who studied natural convection of nanofluid in a differentially heated cavity using Buongiorno's model [36] (see Fig. 3). It can be seen that the present results are in satisfactory agreement with the numerical results of Das et al. [8] and Sheikhzadeh et al. [48].

5. Results and Discussion

The problem of conjugate natural convection heat transfer of nanofluid in a square enclosure containing a conductive partition and several disconnected conducting solid blocks is under study. Results are presented and discussed in terms of streamlines, isotherms, total Nusselt numbers and contour of solid particles distribution for various dominant parameters such as: Rayleigh number ($10^4 \le Ra \le 10^7$), volume fraction ($0 \le \varphi \le 0.05$), diameter ($25nm \le d_p \le 145nm$) and type of the nanoparticles (*Cu*, Al_2O_3 and TiO_2). Moreover, the effects of the design parameters such as: thermal conductivity ratio ($0.1 \le K_r \le 25$), orientation of conductive partition and segmentation of the conductive obstacle on the heat transfer performance of heat exchanger are investigated.

5.1. The effects of the thermal conductivity ratio (K_r)

In this section, the effects of the *Ra*, type of the nanoparticles and thermal conductivity ratio of vertical partition on the fluid flow and heat transfer performance of the heat exchanger are investigated. Figs. 4 and 5 show streamlines and isotherms for both pure water ($\varphi = 0$) and nanofluid ($\varphi = 0.05$) at different *Ra*. Generally, in case 1A, the flow field within the enclosure is characterized by a clockwise eddy due to the temperature difference between the hot and cold

cylinders. Isotherms in Fig. 5 illustrate that at low *Ra*, the mechanism of heat transfer within the enclosure is mainly dominated by the conduction mode, since they are undistorted and almost parallel with vertical walls of the enclosure. In fact, this result is to be expected since under low Rayleigh number conditions, a weak circulation structure is formed, and thus minimal convection heat transfer occurs within the enclosure. As the *Ra* enhances to $Ra = 10^6$ and 10^7, the flow strength increases and streamlines at the center of enclosure become inverted egg-shaped, indicating that convection is the dominant mechanism for heat transfer in the enclosure. Furthermore, Fig. 4 and table 3 demonstrate that by increase the buoyant force via increase in the Rayleigh number, the maximum value of the stream function increases and some other small eddies start to develop near the enclosure walls. Fig. 5 also shows that, due to the stronger convection effects at high *Ra*, thermal boundary layer thickness around the hot and cold cylinders decreases and isotherms become more distorted. It can be clearly seen that, the thermal boundary layer thickness around the hot cylinder in upper half of the enclosure is considerably higher than those at the lower one which indicates that, most of the heat is released from the hot cylinders which are located in the lower half of the enclosure (see $\overline{Nu}_i$ for each hot and cold cylinder). Another interesting feature is that, in all cases the amount of the heat released by hot cylinders is exactly absorbed by the cold cylinder on the opposite side which is another validation of present study from point of view of heat transfer. Furthermore, the absolute value of maximum stream function in Table 3 clearly demonstrates that by increasing the nanoparticles concentration, the intensity of buoyancy and hence the flow intensity decrease and consequently the isotherm pattern becomes more uniform. It can be attributed to the fact that, the presence of nanoparticles will make the nanofluid to be more viscous, which will reduce convection currents and accordingly diminish the temperature gradient. However, Figs. 4 and 5 illustrate that at

constant *Ra*, by locating a full vertical partition at the center of enclosure, the main vortex breaks into two eddies and consequently isotherms become less densely packed adjacent to the heated surfaces especially at low value of thermal conductivity ratio ($K_r = 0.2$) which indicate that convection heat transfer is almost suppressed within the enclosure and conduction mode of heat transfer is coming into picture. Under this condition, isotherms are vertically stratified inside the conductive partition and heat trapping occurs within the enclosure so that heat can only transfer through conduction mode even at high values of *Ra*. The effects of this event can be clearly seen from Fig. 5 where $\overline{Nu}_i$ inside the each heater and cooler macroscopically demonstrates that, the increase of the *Ra* has a nominal impact on the isotherms pattern and heat transfer rate within the enclosure. To better understand the effects of thermal conductivity ratio (K_r) on the heat transfer rate, Fig. 6 is presented where the total Nusselt number is depicted at different *Ra* for case 1A and 1B.

It is evident from Fig. 6 that the total Nusselt number enhances with increase in *Ra*, but the tendency is much affected by presence of the conductive partition. As an example, the values of $\overline{Nu}_{tot}$ in case 1A at $Ra=10^4$, 10^5, 10^6, and 10^7 are respectively 2.51, 6.86, 12.53 and 19.71 times higher than those of the case 1B with K_r=0.2 which indicate that conductive partition with low thermal conductivity acts like insulator. However, table 3 and Fig. 6 demonstrate that as the thermal conductivity ratio enhances, the total Nusselt number and magnitudes of the stream functions ($|\psi_{\max}|$) corresponding to the primary vortices increase which implies that the convection process becomes stronger and heat trapping within the enclosure starts to disappear so that heat can easily transfer through the conductive partition. For instance, at $\varphi = 0$ with the increment of thermal conductivity ratio from $K_r = 1 \text{ to } K_r = 5$ the $\overline{Nu}_{tot}$ augments approximately

around the 22%, 24%, 47% and 76% at Ra=10^4, 10^5, 10^6 and 10^7 respectively while with further increase in thermal conductivity ratio from K_r=5 to K_r=25 this trend is continued by 4%, 2%, 8% and 17%. These values clearly demonstrates that, although by the increment of the thermal conductivity ratio (K_r), total Nusselt number enhances but at each values of Ra, the certain value of K_r exists which beyond that with further increase in K_r the heat transfer rate doesn't alter remarkably. Fig. 6 also shows the effects of the volume fraction and type of the nanoparticles on the total Nusselt number. It can be seen that by increasing the volume fraction of the nanoparticles the total Nusselt number first enhances up to optimum value (φ_{opt}) and then decreases with further increase in the nanoparticles concentration. In fact, Fig. 6 shows that for any given particle type, there is an optimum value of particle concentration that results in the highest heat transfer rate within the heat exchanger. This behavior can be explained by two counter-acting effects: a favorable effect driven by the presence of high thermal conductivity of nanoparticles, and an undesirable effect promoted by the high level of viscosity experienced at the high volume fractions of nanoparticles. Another interesting feature to be observed is that, at low Ra, type of the nanoparticles has a significant impact on the heat transfer rate while at high Ra, this course of the event doesn't observe. The reason is that at low Rayleigh numbers, the heat transfer is dominant by conduction mode. Thus, the addition of nanoparticles with high thermal conductivity such as Cu ($k = 400$) into the pure water will increase the conduction and therefore make the enhancement more effective. However, for intermediate value of Rayleigh number ($Ra = 10^5$) all types of the nanoparticles show somewhat adverse effect on the total Nusselt number in case 1A so that by increasing the volume fraction of the solid particles, the total Nusselt number enhances slightly up to optimum value and then drops immensely with further increase in nanoparticles concentration ($\varphi > \varphi_{opt}$). It can be attributed to the fact that at this

special Rayleigh number ($Ra = 10^5$), heat is transported simultaneously through both conduction and convection mechanisms. Since the addition of nanoparticles to the base fluid enhances the effective viscosity of working fluid, the transformation of the heat transfer mechanism from conduction to convection is postponed to higher value of *Ra* and consequently the heat transfer rate decreases. In the other word, Fig. 6 illustrates that at $Ra = 10^5$ for case 1A, pure water has a considerably better heat transfer performance than the nanofluid at high nanoparticles concentration. However, a different trend can be observed in case 1B where a vertical conductive partition is located at the middle of the enclosure. More precisely, at low value of thermal conductivity ratio ($K_r \le 1$), with a steady increase in nanoparticles concentration the heat transfer rate enhances so that optimum particles loading occurs at $\varphi_{opt} = 0.05$. This kind of the behavior can be explained by the fact that at $K_r \le 1$, the heat transfer is purely due to conduction and viscous forces are dominating. Under this circumstance, addition of the solid particles with high thermal conductivity into the pure fluid is in favor of heat transfer enhancement which leads to improve the overall heat transfer rate within the enclosure. However, as the thermal conductivity ratio enhances, the intensity of the recirculation patterns increases which indicates that the viscous forces become weak in the flow and subsequently the convection current starts to appear within the enclosure. In this case, similar to case 1A, the negative effects of the viscosity enhancement become more visible and compensate the positive effects of the thermal conductivity rise, resulting in a reduction of optimum particles loading from $\varphi_{opt} = 0.05$ to $\varphi_{opt} = 0.03$ (see Fig. 6 at $K_r \ge 5$ and $Ra \ge 10^6$).

Figs. 7 and 8 depict the effects of the *Ra* on the distribution of nanoparticles for cases 1A and 1B. The general view of the figures demonstrates that at high values of *Ra*, deviation of

nanoparticles concentration from its initial value ($\varphi_{opt} = 0.05$) is negligible which indicates that considering the nanofluid as a homogeneous solution seems to be reasonable where natural convection regime is dominant. However, as the *Ra* decreases, the strength of circulating cells reduces and therefore a degree of non-uniformity can be observed in the distribution of the solid particles. The reason is that, at low *Ra*, the fluid circulation within the enclosure is very weak so that the solid particles have a mighty chance to escape from the core circulation region and deposit on the rigid walls. However, as the Rayleigh number increases to 10^7, the strength of the main vortex gets enhanced via increase in the buoyancy force; therefore, more particles are captured by the circulating flow and stay away from the rigid walls which reduces their deposition chance. In addition, it can be seen that at the constant *Ra*, by inserting a conductive partition into the enclosure, the distribution of solid particles becomes more non uniform. As discussed before, presence of the conductive wall in the enclosure (case 1B) leads to a significant reduction in the flow intensity and accordingly maximum stream function (see table 3). In fact, decrease in the flow intensity gives the solid particles the chance to escape from the main vortex, resulting in higher deposition rate within the enclosure. Figs. 7 and 8 also show that by decreasing the thermal conductivity of the nanoparticles (through changing type of them from *Cu* (k=400) to TiO_2 (k=8.9)) distribution of solid particles becomes more none-uniform. This physical behavior can be explained by the fact that, according to Eq. (8), by decreasing the thermal conductivity of the nanoparticles (k_p), the effects of the theromophoresis force increases, resulting in a significant increment in the magnitude of the slip velocity between two phases. As the slip velocity between liquid and solid phase increases, distribution of solid particles becomes more non-uniform, resulting in a considerable variation in local thermal conductivity and viscosity of the working fluid (nanofluid) within the enclosure. In fact, these observations can be

another reason to explain why at low *Ra*, type of the solid particles has a big impact on the total Nusselt number and optimum volume fraction of the nanoparticles.

5.2. Orientation of the conductive partition

In this section the effects of the *Ra*, nanoparticles diameter and orientation of the conductive wall on the fluid flow and heat transfer characteristics of nanofluids are presented.

Figs. 9 and 10 illustrate the effects of orientation of the conductive partition on the streamline and isotherms at different *Ra*. Similar to previous section due to temperature differences between the hot and cold surfaces, the fluid near the heater has lower density than those near cold surfaces on the right wall of the enclosure. As a result, the heated fluid ascends along the heaters then it is cooled and descends at the vicinity of the discrete cold surfaces and hence a primary clockwise vortex is established inside the enclosure in case 2A. It can be seen from Fig. 10 that at low *Ra*, isotherms are uniform and parallel to each other which indicates that conduction heat transfer is dominant. As *Ra* increases to 10^5, intensity of the recirculation patterns enhances and subsequently the absolute values of stream functions increase (see table 4). At this *Ra*, the distinct thermal boundary layers are formed adjacent to the isothermal surfaces which indicate that transient point from conduction to convection mode takes place at this *Ra*. As *Ra* increases to 10^6, the buoyancy forces start dominating on viscous forces and isotherms become distorted. Isotherms in Fig. 10 also show that by increasing in the *Ra*, thermal boundary layer on the surface of the heated cylinders becomes thinner so that a thermal plume starts to form on top of the hot cylinders which indicate that the isotherms move upward, giving rise to a stronger temperature gradient in the bottom and left parts of the heater and much lower thermal gradient in the right and top areas where convection heat transfer is considerably weaker compare to other

areas. It is also apparent that the presence of the solid particles into the pure fluid results in the drop of the convection process in the isotherms as the curved shape of the isotherms changes to linear ones and also their movements within the enclosure decrease immensely (see also table 4). Furthermore, Figs. 9 and 10 demonstrate how flow pattern and temperature field are influenced by inserting vertical (case 2B), horizontal (case 2C) and plus-shaped (case 2D) partitions into the enclosure. As listed in table 4, in general, insertion of conductive wall inside the enclosure restricts flow circulation and consequently causes significant drop in convective heat transfer across the whole enclosure. This decrease in the flow movement is accompanied by an increase in the thermal diffusivity and thermal boundary layer thickness, resulting in a significant drop in the temperature gradients adjacent to the heated walls and heat transfer rate accordingly. The effects of this event can be clearly seen from Fig. 10 where isotherms are more diffused inside the enclosure and size of the thermal plume around the hot cylinders decreases which implies that transition from conduction to convection heat transfer is postponed from Ra=10^5 to 10^6 especially in case 2B and 2D. In fact, due to occurrence of heat-trapping phenomenon in these cases, the fluid flow is almost stagnant in the bulk of the enclosure interior which indicates that buoyancy force cannot overcome the viscous force and subsequently the heat transfer mechanism occurs through the conduction even at Ra=10^5. This rather intriguing behavior can be better understood by scrutinizing Fig. 11 where the effects of the Ra and orientation of the partitions are presented for case 2A to 2D. It is evident from Fig. 11 that orientation of the conductive partition has a significant impact on the heat transfer rate for cases 2B and 2C. Take as an illustration, the total Nusselt number in case 2A for pure fluid ($\varphi = 0$) at Ra=10^4, 10^5, 10^6 and 10^7 are respectively: 1.58, 2.27, 2.33 and 2.44 times higher than the case 2B while this trend is continued by 1.27, 1.35, 1.08 and 1.02 between case 2A and case 2C. It is interesting to note that,

these values increase considerably between case 2A and 2D where both vertical and horizontal conductive walls are located within the enclosure. This physical behavior can be explained by the fact that in cases 2B and 2D, heat trapping occurs within the enclosure so that the working fluid can only circulate adjacent to either hot or cold surfaces whereas in case 2C, the working fluid is in contact with both heater and cold surface which are located in each row. This reason explains why at high *Ra*, the values of $\overline{Nu}_{tot}$ in cases 2A-2C and 2B-2D are very close together. Moreover, another interesting observation which is worth mentioning is that although at high *Ra*, insertion of the horizontal conductive partition has a small impact on the overall heat transfer rate ($\overline{Nu}_{tot}$) within the enclosure but it significantly influence the average Nusselt number ($\overline{Nu}_{i}$) for each hot and cold surfaces. For instance, at $Ra=10^7$ the average Nusselt number for each heater in case 2A are $\overline{Nu}_{total\ case2A}=17.73$, $\overline{Nu}_{bottom\ heater}=13.2$ and $\overline{Nu}_{top\ heater}=4.53$ while these values are $\overline{Nu}_{total\ case2C}=17.52$, $\overline{Nu}_{bottom\ heater}=11.2$ and $\overline{Nu}_{top\ heater}=6.32$ for case 2C. These values clearly demonstrate that, in case 2A at $Ra\geq 10^6$, the amount of heat released by the bottom heater is significantly higher than the top one which indicates that this heater plays a vital role in the heat transfer mechanism within the enclosure while upper heater remains comparatively inactive and contributes much to flow inhibition (see $\overline{Nu}_{i}$, as labeled in isotherms inside the each heater). However, by locating the horizontal conductive partition into the enclosure (case 2B) this scenario alters significantly so that $\overline{Nu}_{i}$ for the bottom heater decreases and role of the upper heater becomes more visible. In fact, this interesting point can be concluded that, orientation of the conductive partition can be used as a control parameter for the heat and fluid flow around the each heater while overall heat transfer rate across the whole enclosure will remain constant.

Fig. 11 also shows the effects of the volume fraction and size of the nanoparticles on the total Nusselt number. Similar to previous section, the total Nusselt number initially increases to a maximum and then it decreases rapidly with augment of nanoparticles concentration. As mentioned before, adding nanoparticle to the base fluid has two opposite influences on the heat transfer rate: a positive effect due to their potential in enhancement of effective thermal conductivity and negative effect due to excessive growth of the effective dynamic viscosity. The negative effect of the viscosity enhancement is demonstrated in table 4 where absolute values of maximum stream function ($|\psi_{\max}|$) illustrate how strength of the flow is influenced by the addition of nanoparticles into the pure fluid. It can be seen from table 4 that, flow intensity decreases as long as the volume fraction of the nanofluid increases, which means that, the flow penetrating into the enclosure decreases with increase of the volume fraction. Furthermore, higher values of effective viscosity of nanofluid are accompanied by higher values of thermal diffusivity. The high value of thermal diffusivity causes a drop in the temperature gradients and accordingly enhances the thermal boundary thickness as demonstrated in Fig. 10. This increase in thermal and momentum boundary layer thickness reduces the Nusselt number. On the other hand, according to the equations of (13) and (18), there is a direct correlation between effective thermal conductivity, nanoparticles concentration and Nusselt number so that by increasing solid volume fraction, the thermal conductivity of nanofluid enhances which leads to increase in the heat transfer rate. In fact, optimum particle loading (φ_{opt}) specifies the certain volume fraction of solid particles where the thermal balance occurs between these two opposite factors within the enclosure. More precisely, at $\varphi < \varphi_{opt}$ the enhancement in effective dynamic viscosity due to the presence of nanoparticles is much smaller than thermal conductivity ratio therefore an enhancement in Nusselt number is taken place by increasing the volume fraction of

nanoparticles. However, at $\varphi_{opt} < \varphi$ the high level of viscosity at high volume fractions of nanoparticles becomes more dominant, which reduces the enhancement promoted by the high thermal conductivity and consequently heat transfer rate decreases as a nanoparticles concentration increases. Moreover, Fig. 11 reveals that by increasing the size of the solid particles, the heat transfer rate and φ_{opt} decreases. Similar observations were reported by Corcione et al. [49] who investigated the effects of the nanoparticles size on the heat transfer performance of nanofluid in closed enclosure.

Following correlations can be obtained from numerical simulations to estimate the value of $\overline{Nu}_{tot}$ as a function of Rayleigh number ($10^4 \le Ra \le 10^7$), the volume fraction ($0 \le \varphi \le 0.05$) and the size of nanoparticles ($25nm \le d_p \le 145nm$):

$$\overline{Nu}_{tot} = 0.152\ (1+\varphi^{0.58}(\frac{d_p}{d_f})^{-0.11} e^{-14.72\varphi})\ Ra^{0.298} \tag{19}$$

Fig. 12 depicts the effects of the orientation of the conductive wall on the nanoparticle concentration at different *Ra* for cases 2A to 2D. Similar to previous section, a non-uniform nanoparticle distribution can be observed for lower values of Rayleigh number because of the very weak convective flow in the enclosure. In contrast, as the *Ra* enhances, buoyancy force increases and takes control of nanoparticle concentration, and prevents formation of concentration gradients so that the non-homogeneous areas become more and more confined close to the boundaries and the homogeneous area increases in size until it occupies most part of the enclosure (i.e. nanoparticle distribution becomes uniform). Fig. 12 also reveals that due to suppression effects of the conductive partition on the convection current and flow intensity, distribution of the solid particles in cases 2B, 2C and 2D is relatively higher than the case 2A (especially at low values of *Ra* where conduction mode of the heat transfer is dominant). Finally,

it can be seen that the nanoparticle concentration is higher near the cold wall (nanoparticles' accumulation) whereas its minimum value occurs at the vicinity of the heaters (nanoparticles' depletion); that is, the nanoparticles migrate from the hot region toward the cold one. It can be attributed to the fact that, temperature differences between hot and cold surfaces within the enclosure impose a temperature gradient (∇T) in the nanofluid which consequently creates a thermophoretic force according to Eq. (8). The thermophoretic force then pushes the solid particles from the hot region to the cold one (in the direction of the heat transfer), leading to a region with very large viscosity and thermal conductivity, whereas a reverse trend can be observed around the heaters.

5.3. Segmentation of the conductive obstacle

Figs. 13 and 14 demonstrate the effects of the *Ra* and segmentation of the conductive obstacle on the streamline and isotherms for case 3A to 3D. It should be noted that in this section, the subdivision of the conductive block is carried out in such a way that the amount of solid constituent within the enclosure remains constant. For example, the solid-to-fluid volume ratio (γ) in cases 3B ($\gamma = 0.2$, $N_B = 1$, $L_1 = L_2 = 0.45$), case 3C ($\gamma = 0.2$, $N_B = 4$, $L_1 = L_2 = 0.225$), and case 3D ($\gamma = 0.2$, $N_B = 9$, $L_1 = L_2 = 0.15$) are equal to each other, which permits a proper comparison between cases. Generally, the buoyant forces generated due to the fluid temperature differences between hot and cold surfaces causes the heated fluid ascends along the left wall then moves horizontally towards the right vertical wall of the enclosure. Then, the fluid is cooled and descends at the vicinity of the cold surfaces, and hence a clockwise circulating cell is developed inside the heat exchanger. It can be observed that by increasing the *Ra*, the central stream line is elongated and some other secondary vertices appear inside the enclosure and their

intensity increases as the buoyant force becomes stronger. As illustrated in the table 5 at $Ra \geq 10^6$ the existence of suspended nanoparticles in the base fluid does not affect the maximum stream function significantly while at $Ra \leq 10^5$ the strength of the flow within the enclosure evidently decreases with increase in viscosity of nanofluid via increase in the nanoparticles concentration. Fig. 14 also demonstrates a conduction-dominated regime with vertical isotherms at low Rayleigh numbers and a convection dominated regime with horizontal isotherms at high Rayleigh numbers. It can be seen from the figures that at high *Ra*, distinct thermal boundary layers are formed at the vicinity of all hot and cold surfaces while the core of the enclosure is thermally stratified which indicate that the flow is almost stagnant in the bulk of the enclosure interior except at portions close to the vertical walls. It is surprising to find that in all cases, the amount of the heat releases from hot surface in lower part of the enclosure is significantly higher than the top one while a reverse trend is observed for the cold surfaces. Another interesting feature is that, the amount of the heat released by bottom left source is sent to the top right sink and the heat from the top left source is transported to the bottom right sink as indicated by the average Nusselt number values ($\overline{Nu}_i$). In fact, Fig 14 reveals that the heat transfer relationship between sources and sinks, in terms of the average Nusselt number values, is one to one in a reversed manner. Similar observation was reported by Deng et al. [6] who investigated the effects of the location and segmentation of the hot and cold surfaces on the heat transfer rate within the enclosure. However, Fig. 14 and table 5 demonstrate that at a constant *Ra* by locating a conductive obstacle at the center of the enclosure (case 3B) and dividing it into the small segments (case 3C and 3D), the values of the maximum stream function decrease and the isotherms become vertically stratified in the central part of the domain region where the fluid circulation is consequently weakened. However, in the vicinity of the differentially heated

walls, the isotherms are still considerably distorted and tightened because of the significant heat exchange between these walls and the fluid. The corresponded streamlines in Fig. 13 illustrate that the flow structures is obviously affected by the fragmentation of the solid blocks. More precisely, in all cases the main circulation of the flow is formed between the peripheral blocks and walls of the enclosure while a circulation of less importance is established between the conductive blocks and loses of importance by increasing Rayleigh number. Such behavior can be better understood by scrutinizing Fig. 15 where variation of total Nusselt number are depicted for various values of Rayleigh number, and volume fraction of nanofluid.

It can be seen from Fig. 15 that the effects of the segmentations of the conductive obstacle are more pronounced at low *Ra* where conduction heat transfer is dominant. As an example, at $Ra=10^4$ for $\varphi = 0$ ratios of total Nusselt number for case 3A over that of cases 3B, 3C and 3D are; 1.05, 2.56 and 2.65 while these values at $Ra=10^7$ are 1.001, 1.006 and 1.01, respectively. These values clearly indicate that the effect of the fragmentation on the heat transfer rate is very important at low and moderate Rayleigh numbers ($Ra \le 10^5$) where buoyancy and viscous forces are comparable but this effect is reduced at high *Ra* where viscous forces are no more in the flow and only buoyancy forces are leading the flow. It can be attributed to the fact that at low *Ra*, by dividing the solid obstacles into the small parts, the flow intensity decreases significantly whereas this course of the event doesn't occur at high *Ra*. For example, for the pure fluid ($\varphi = 0$) at $Ra=10^4$ the $|\psi_{\max}|$ in case 3A are respectively 2.09, 5.64 and 6.9 times higher than those associated with cases 3B, 3C and 3D while these values at $Ra=10^7$ are 1.11, 1.02 and 1.03, respectively. Fig. 15 also reveals that, by increasing the size of the nanoparticles, φ_{opt} and heat transfer rate decreases. Generally, the effect of particle size on the heat transfer enhancement in nanofluids can be explained by two factors: Brownian motion due to motion of

nanoparticles that transports heat (diffusion of nanoparticles) and micro-convection induced by Brownian motion. More precisely, according to Eq. (13) by decreasing the diameter of the nanoparticles, the effects of the Brownian motion (Re_B) enhances which in turn leads to increase in the effective thermal conductivity of the nanofluid and heat transfer rate accordingly. Interestingly, it can be observed from Fig. 15 that at $Ra = 10^5$ where transition point from conduction to convection mode occurs within the enclosure, the addition of the nanoparticles into the pure fluid has a minor or even negative impact on the heat transfer rate.

Fig. 16 reveals the effects of the *Ra* and segmentation of the conductive obstacles on the nanoparticles distribution. Similar to previous sections, it can be seen that concentration of the nanoparticles in the close vicinity of the cold surfaces is slightly higher than that of the hot ones. As mention before, at low values of *Ra*, thermophoresis is the main mechanism of nanoparticle migration which tends to move solid particles in the direction opposite to the temperature gradient so that solid particles migrate from the hot region (making a depleted region) and accumulate on the cold walls. As a result of this event, at low *Ra*, a degree of heterogeneity of nanoparticles concentration occurs within the enclosure, resulting in a non-uniform distribution of local thermo physical properties of nanofluids. In fact, due to the strong impact of nanoparticle concentration on the effective thermal conductivity and viscosity, the heat transfer rate and optimum particles loading show great sensitivity to changes in particles diameter at low *Ra*. However, as the *Ra* enhances, circulation in the enclosure becomes stronger, and therefore more particles are captured by the circulating flow and cannot escape from the high intensity core circulation region and deposit on the walls. In fact, Fig. 16 reveals that under this circumstance, the homogenous assumption in simulation of natural convection heat transfer of nanofluids is correct and reliable. Moreover, Fig. 16 interestingly demonstrates that, similar to

streamlines (see Fig. 13), isotherms (see Fig. 14) and average Nusselt number (see $\overline{Nu}_i$ in Fig. 14), an inverse one-to-one relationship also occurs in the nanoparticles concentration so that the depletion of the solid particles in a particular area is reversely corresponded to the accumulation of the nanoparticles in the opposite side. In fact, this phenomenon can be considered as another validation of the present study from the movement of thermal energy and conservation of volume fraction (nanoparticles distribution) point of view. Finally, Fig. 16 reveals that, unlike the full partitioning the enclosure, presence of the solid obstacles inside the enclosure and dividing them into the smaller segments have negligible impact on the distribution of the solid particles.

6. Conclusions

This study investigates the conjugate natural convection of nanofluid in a square enclosure containing a conductive partition and several disconnected conducting solid blocks. The effect of the pertinent parameters such as; the Rayleigh number, volume fraction, diameter and type of the nanoparticles, thermal conductivity ratio, orientation of conductive partition and segmentation of the conductive obstacle on the heat transfer performance of the nanofluid have been investigated and following results are obtained:

- The results show that, orientation of the conductive partition can be used as a control parameter for the heat and fluid flow within the heat exchangers.
- It is found that by increasing the *Ra* and thermal conductivity ratio (K_r) of vertical partition, the total Nusselt number increases. However, at each values of *Ra*, the certain value of K_r exists which beyond that with further increment of K_r the heat transfer rate doesn't alter remarkably.

- The results show that at low *Ra*, by subdividing the conductive obstacle into the small segments, the total Nusselt number decreases significantly while at high *Ra*, this course of the event doesn't occur.
- The results show that at moderate Rayleigh number ($Ra=10^5$), pure water has a slightly better heat transfer performance than the nanofluid with $\varphi = 5\%$.
- One of the fundamental results is that at each *Ra*, the optimal particle loading (φ_{opt}) exists which beyond that with further increase in the nanoparticles concentration, the total Nusselt number decreases.
- The results show that at low *Ra*, the heat transfer rate is very sensitive to size and type of the nanoparticles so that by decreasing the diameter of solid particles, the optimal particle loading increases.
- It is found that, by decreasing the thermal conductivity of the nanoparticles (through changing type of them from *Cu* (*k*=400) to TiO_2 (*k*=8.9)) distribution of solid particles becomes more none-uniform.
- The results show that, thermophoresis is the main mechanism of nanoparticle migration which tends to move solid particles in the direction opposite to the temperature gradient so that solid particles migrate from the hot region (making a depleted region) and accumulate on the cold walls.
- The results show that, by adding the nanoparticles with concentration of 5% into the base fluid, strength of the recirculating cell decreases and isotherm pattern becomes more uniform.
- It is found that at the constant *Ra*, by inserting a full vertical partition into the enclosure, non-uniformity in the distribution of the solid particles becomes more severe.

- The results show that, the presence of several disconnected conducting solid blocks inside the enclosure has a minor impact on the nanoparticles distribution.

In the future works, the effects of the location, thickness and number of the conductive partitions on the flow filed and heat transfer characteristic can be investigated. Moreover, the study can be extended for turbulent flow with different thermal boundary conditions such as constant heat flux with radiation. Finally, many other factors such as shape of the particles, micro-convection, pH value, and the particle-particle interactions may have important influence on the heat transfer performance of the nanofluids in natural convective heat transfer, which can be identified further in future work.

Acknowledgments

The authors would like to thank anonymous reviewers for their helpful and constructive comments that greatly helped us to improve the final version of the paper.

References

[1] C.J. Ho, W. Chang, C. Wang, Natural Convection Between Two Horizontal Cylinders in an Adiabatic Circular Enclosure, J. Heat Transfer. 115 (1993) 158–165.

[2] C.S. Dai, M. Li, H.Y. Lei, S.X. Wang, Numerical simulation of natural convection between hot and cold microtubes in a cylinder enclosure, Int. J. Therm. Sci. 95 (2015) 115–122.

[3] F. Garoosi, M.R. Safaei, M. Dahari, K. Hooman, Eulerian–Lagrangian analysis of solid particle distribution in an internally heated and cooled air-filled cavity, Appl. Math. Comput. 250 (2015) 28–46.

[4] Y. Gap, H. Sik, M. Yeong, Natural convection in square enclosure with hot and cold cylinders at different vertical locations, Int. J. Heat Mass Transf. 55 (2012) 7911–7925.

[5] Q.X. Wang, H.Y. Lei, S.X. Wang, C.S. Dai, Natural convection around a pair of hot and cold horizontal microtubes at low Rayleigh numbers, Appl. Therm. Eng. 72 (2014) 114–119.

[6] Q.-H. Deng, Fluid flow and heat transfer characteristics of natural convection in square cavities due to discrete source–sink pairs, Int. J. Heat Mass Transf. 51 (2008) 5949–5957.

[7] H.F. Oztop, Y. Varol, A. Koca, Natural convection in a vertically divided square enclosure by a solid partition into air and water regions, Int. J. Heat Mass Transf. 52 (2009) 5909–5921.

[8] M.K. Das, K.S.K. Reddy, Conjugate natural convection heat transfer in an inclined square cavity containing a conducting block, Int. J. Heat Mass Transf. 49 (2006) 4987–5000.

[9] A. Raji, M. Hasnaoui, M. Naïmi, K. Slimani, M.T. Ouazzani, Effect of the subdivision of an obstacle on the natural convection heat transfer in a square cavity, Comput. Fluids. 68 (2012) 1–15.

[10] J.-T. Hu, X.-H. Ren, D. Liu, F.-Y. Zhao, H.-Q. Wang, Conjugate natural convection inside a vertical enclosure with solid obstacles of unique volume and multiple morphologies, Int. J. Heat Mass Transf. 95 (2016) 1096–1114.

[11] Q. Ren, C.L. Chan, Natural convection with an array of solid obstacles in an enclosure by lattice Boltzmann method on a CUDA computation platform, Int. J. Heat Mass Transf. 93 (2016) 273–285.

[12] M. Khatamifar, W. Lin, S.W. Armfield, D. Holmes, M.P. Kirkpatrick, Conjugate natural convection heat transfer in a partitioned differentially-heated square cavity, Int. Commun. Heat Mass Transf. 81 (2017) 92–103.

[13] S.M. Vanaki, P. Ganesan, H.A. Mohammed, Numerical study of convective heat transfer of nano fl uids : A review, Renew. Sustain. Energy Rev. 54 (2016) 1212–1239.

[14] F. Selimefendigil, H.F. Öztop, Analysis of MHD mixed convection in a flexible walled and nanofluids filled lid-driven cavity with volumetric heat generation, Int. J. Mech. Sci. 118 (2016) 113–124.

[15] F. Selimefendigil, H.F. ??ztop, Conjugate natural convection in a cavity with a conductive partition and filled with different nanofluids on different sides of the partition, J. Mol. Liq. 216 (2016) 67–77.

[16] F. Selimefendigil, H.F. Öztop, Influence of inclination angle of magnetic field on mixed convection of nanofluid flow over a backward facing step and entropy generation, Adv. Powder Technol. 26 (2015) 1663–1675.

[17] F. Selimefendigil, H.F. ??ztop, MHD mixed convection of nanofluid filled partially heated triangular enclosure with a rotating adiabatic cylinder, J. Taiwan Inst. Chem. Eng. 45 (2014) 2150–2162.

[18] M. Sheikholeslami, D.D. Ganji, S. Soleimani, Effect of a magnetic field on natural convection in an inclined half-annulus enclosure filled with Cu – water nanofluid using CVFEM, Adv. Powder Technol. 24 (2013) 980–991.

[19] M. Sheikholeslami, M. Gorji-Bandpy, D.D. Ganji, Lattice Boltzmann method for MHD natural convection heat transfer using nanofluid, Powder Technol. 254 (2014) 82–93.

[20] M. Sheikholeslami, D.D. Ganji, Free convection of Fe 3 O 4-water nanofluid under the influence of an external magnetic source, J. Mol. Liq. 229 (2017) 530–540.

[21] G.H.R. Kefayati, Heat transfer and entropy generation of natural convection on non-Newtonian nano fl uids in a porous cavity, Powder Technol. 299 (2016) 127–149.

[22] G.H.R. Kefayati, N. Azwadi, C. Sidik, Simulation of natural convection and entropy generation of non-Newtonian nanofluid in an inclined cavity using Buongiorno ' s mathematical model (Part II , entropy generation), Powder Technol. 305 (2017) 679–703.

[23] G.R. Kefayati, Mesoscopic simulation of magnetic field effect on double-diffusive mixed convection of shear-thinning fluids in a two sided lid-driven cavity, J. Mol. Liq. 198 (2014) 413–429.

[24] G.H.R. Kefayati, Mesoscopic simulation of mixed convection on non-Newtonian nanofluids in a two sided lid-driven enclosure, Adv. Powder Technol. 26 (2015) 576–588.

[25] A. el malik Bouchoucha, R. Bessaïh, H.F. Oztop, K. Al-Salem, F. Bayrak, Natural convection and entropy generation in a nanofluid filled cavity with thick bottom wall: Effects of non-isothermal heating, Int. J. Mech. Sci. (2017).

[26] M.A. Sheremet, I. Pop, R. Nazar, Natural convection in a square cavity filled with a porous medium saturated with a nanofluid using the thermal nonequilibrium model with a Tiwari and Das nanofluid model, Int. J. Mech. Sci. 100 (2015) 312–321.

[27] V.M. Job, S.R. Gunakala, Mixed convection nanofluid flows through a grooved channel with internal heat generating solid cylinders in the presence of an applied magnetic field, Int. J. Heat Mass Transf. 107 (2017) 133–145.

[28] A.M. Rashad, M.A. Ismael, A.J. Chamkha, M.A. Mansour, MHD mixed convection of localized heat source/sink in a nanofluid-filled lid-driven square cavity with partial slip, J. Taiwan Inst. Chem. Eng. 68 (2016) 173–186.

[29] A. Purusothaman, N. Nithyadevi, H.F. Oztop, V. Divya, K. Al-salem, Three dimensional numerical analysis of natural convection cooling with an array of discrete heaters embedded in nanofluid filled enclosure, Adv. Powder Technol. 27 (2016) 268–280.

[30] C.-C. Cho, C.-H. Chiu, C.-Y. Lai, Natural convection and entropy generation of Al2O3–water nanofluid in an inclined wavy-wall cavity, Int. J. Heat Mass Transf. 97 (2016) 511–

520.

[31] J. Maxwell, A treatise on electricity and magnetism (vol. II), Oxford University Press, Cambridge, 1881.

[32] H.C. Brinkman, The Viscosity of Concentrated Suspensions and Solutions, J. Chem. Phys. 20 (1952) 571–581.

[33] M. Corcione, Empirical correlating equations for predicting the effective thermal conductivity and dynamic viscosity of nanofluids, Energy Convers. Manag. 52 (2011) 789–793.

[34] G. Wang, J. Zhang, Thermal and power performance analysis for heat transfer applications of nanofluids in flows around cylinder, Appl. Therm. Eng. 112 (2017) 61–72.

[35] D. Wen, Y. Ding, Experimental investigation into convective heat transfer of nanofluids at the entrance region under laminar flow conditions, Int. J. Heat Mass Transf. 47 (2004) 5181–5188.

[36] J. Buongiorno, Convective Transport in Nanofluids, J. Heat Transfer. 128 (2006) 240–250.

[37] M.A. Sheremet, I. Pop, N.C. Roşca, Magnetic field effect on the unsteady natural convection in a wavy-walled cavity filled with a nanofluid: Buongiorno's mathematical model, J. Taiwan Inst. Chem. Eng. 61 (2016) 211–222.

[38] M. Esfandiary, B. Mehmandoust, A. Karimipour, Natural convection of Al2O3-water nano fluid in an inclined enclosure with the effects of slip velocity mechanisms : Brownian motion and thermophoresis phenomenon, Int. J. Therm. Sci. 105 (2016) 137–158.

[39] S.Y. Motlagh, H. Soltanipour, Natural convection of Al2O3 -water nano fluid in an inclined cavity using Buongiorno's two-phase model, Int. J. Therm. Sci. 111 (2017) 310–320.

[40] O.K. Koriko, A.J. Omowaye, N. Sandeep, I.L. Animasaun, Analysis of boundary layer formed on an upper horizontal surface of a paraboloid of revolution within nanofluid flow in the presence of thermophoresis and Brownian motion of 29nm CuO, Int. J. Mech. Sci. 124 (2017) 22–36.

[41] A. Malvandi, F. Hedayati, D.D. Ganji, Slip effects on unsteady stagnation point flow of a nanofluid over a stretching sheet, Powder Technol. 253 (2014) 377–384.

[42] A. Malvandi, M.H. Kaffash, D.D. Ganji, Nanoparticles migration effects on magnetohydrodynamic (MHD) laminar mixed convection of alumina/water nanofluid inside microchannels, J. Taiwan Inst. Chem. Eng. 52 (2015) 40–56.

[43] A. Malvandi, S.A. Moshizi, D.D. Ganji, Two-component heterogeneous mixed convection of alumina/water nanofluid in microchannels with heat source/sink, Adv. Powder Technol. 27 (2016) 245–254.

[44] F. Hedayati, A. Malvandi, M.H. Kaffash, D.D. Ganji, Fully developed forced convection of alumina/water nanofluid inside microchannels with asymmetric heating, Powder Technol. 269 (2015) 520–531.

[45] F. Hedayati, G. Domairry, Effects of nanoparticle migration and asymmetric heating on

mixed convection of TiO 2–H 2 O nanofluid inside a vertical microchannel, Powder Technol. 272 (2015) 250–259.

[46] F. Hedayati, G. Domairry, Nanoparticle migration effects on fully developed forced convection of TiO2-water nanofluid in a parallel plate microchannel, Particuology. 24 (2016) 96–107.

[47] H.A. Pakravan, M. Yaghoubi, Analysis of nanoparticles migration on natural convective heat transfer of nanofluids, Int. J. Therm. Sci. 68 (2013) 79–93.

[48] G.A. Sheikhzadeh, M. Dastmalchi, H. Khorasanizadeh, Effects of nanoparticles transport mechanisms on Al2O3–water nanofluid natural convection in a square enclosure, Int. J. Therm. Sci. 66 (2013) 51–62.

[49] M. Corcione, M. Cianfrini, A. Quintino, Enhanced natural convection heat transfer of nanofluids in enclosures with two adjacent walls heated and the two opposite walls cooled, Int. J. Heat Mass Transf. 88 (2015) 902–913.

[50] F.P. Incropera, D.P. DeWitt, Introduction to Heat Transfer, WileyNew York, 2002.

[51] G.S. McNab, A. Meisen, Thermophoresis in liquids, J. Colloid Interface Sci. 44 (1973) 339–346.

[52] S. V. Patankar, Numerical heat transfer and fluid flow, McGraw-Hill, Washington, 1980.

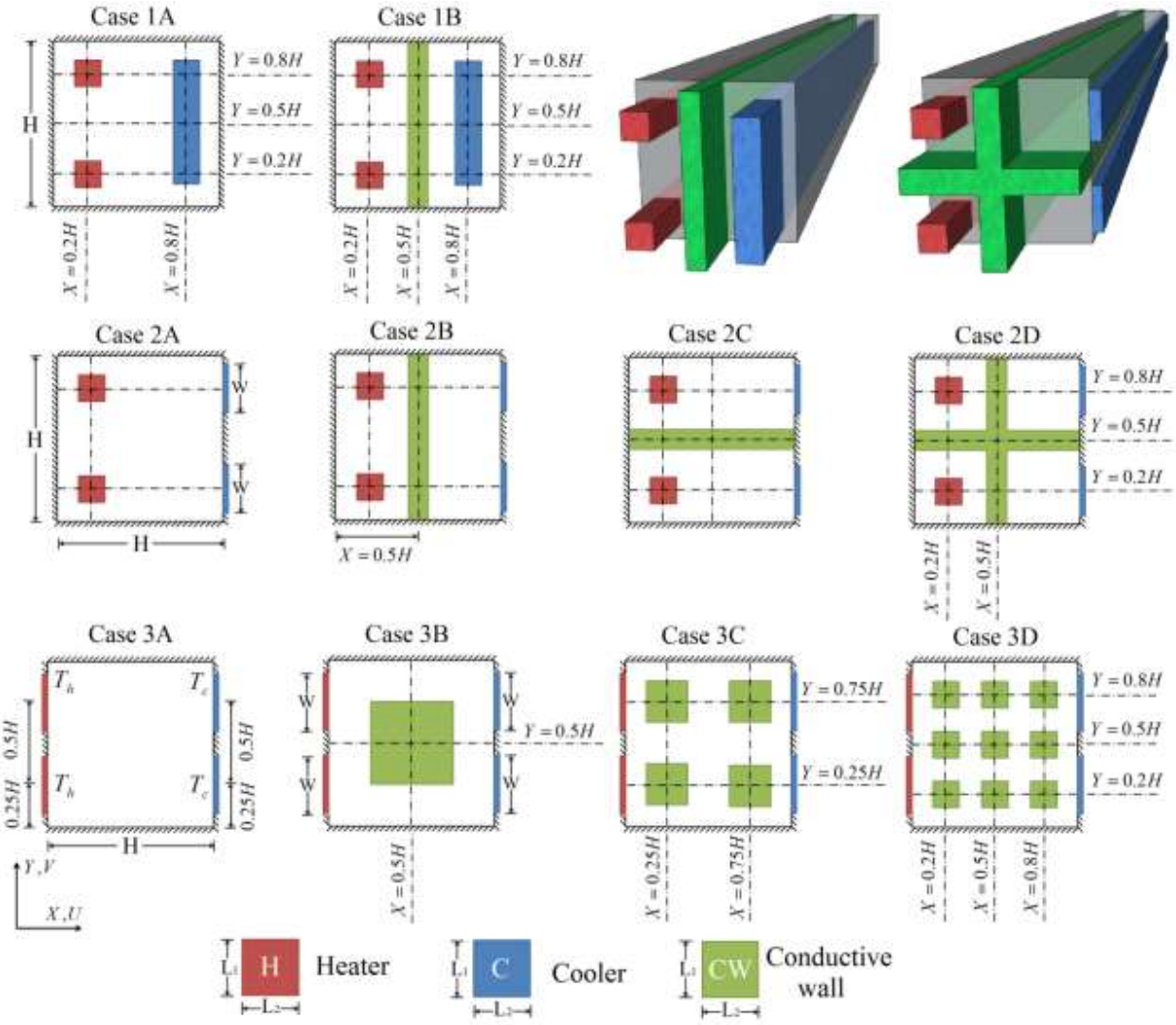

Fig. 1. Schematic diagram of the physical model with boundary conditions.

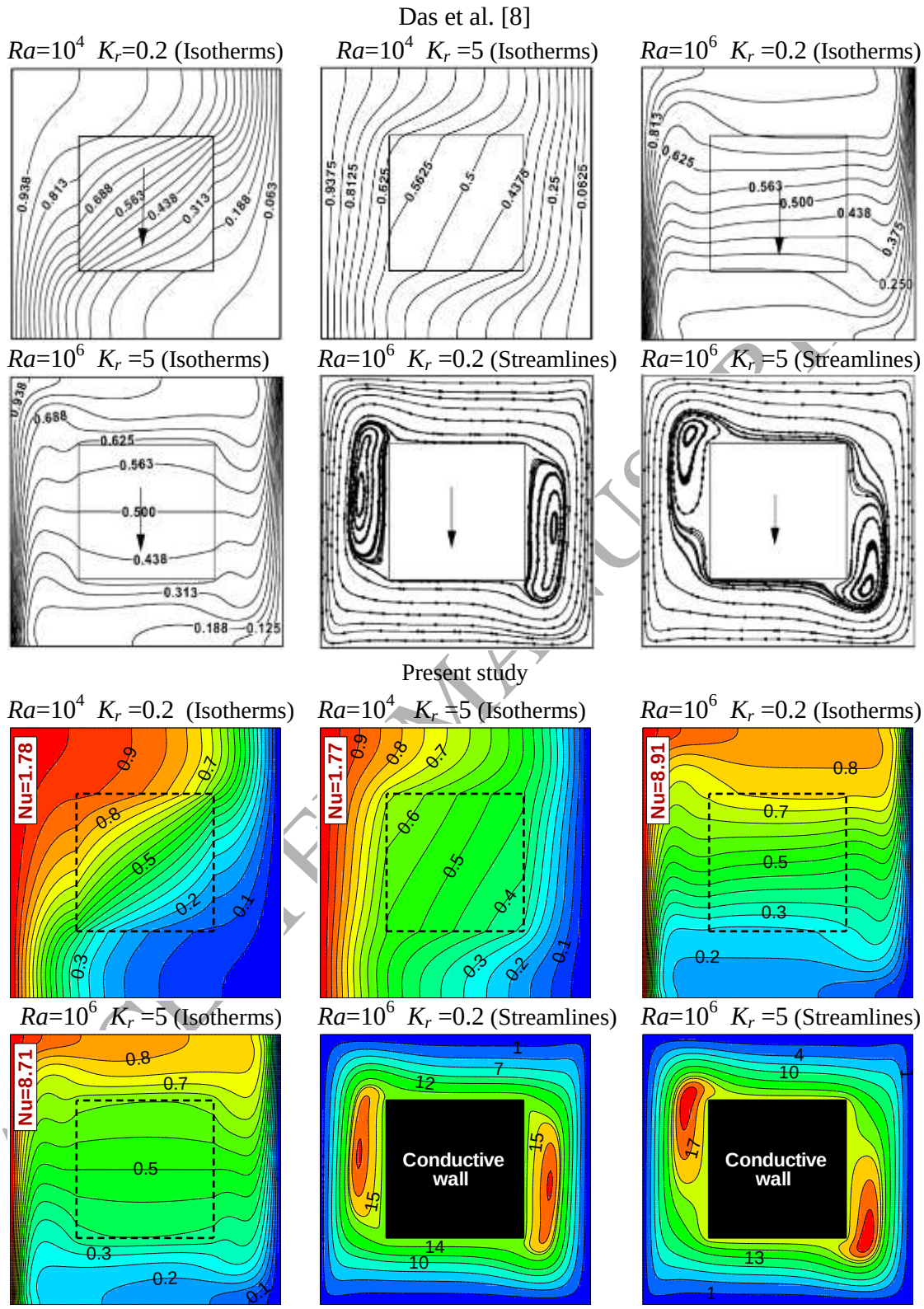

Fig.2. Comparison of the streamlines and isotherms computed by Das et al. [8] and computed with present code for various Rayleigh number and K_r.

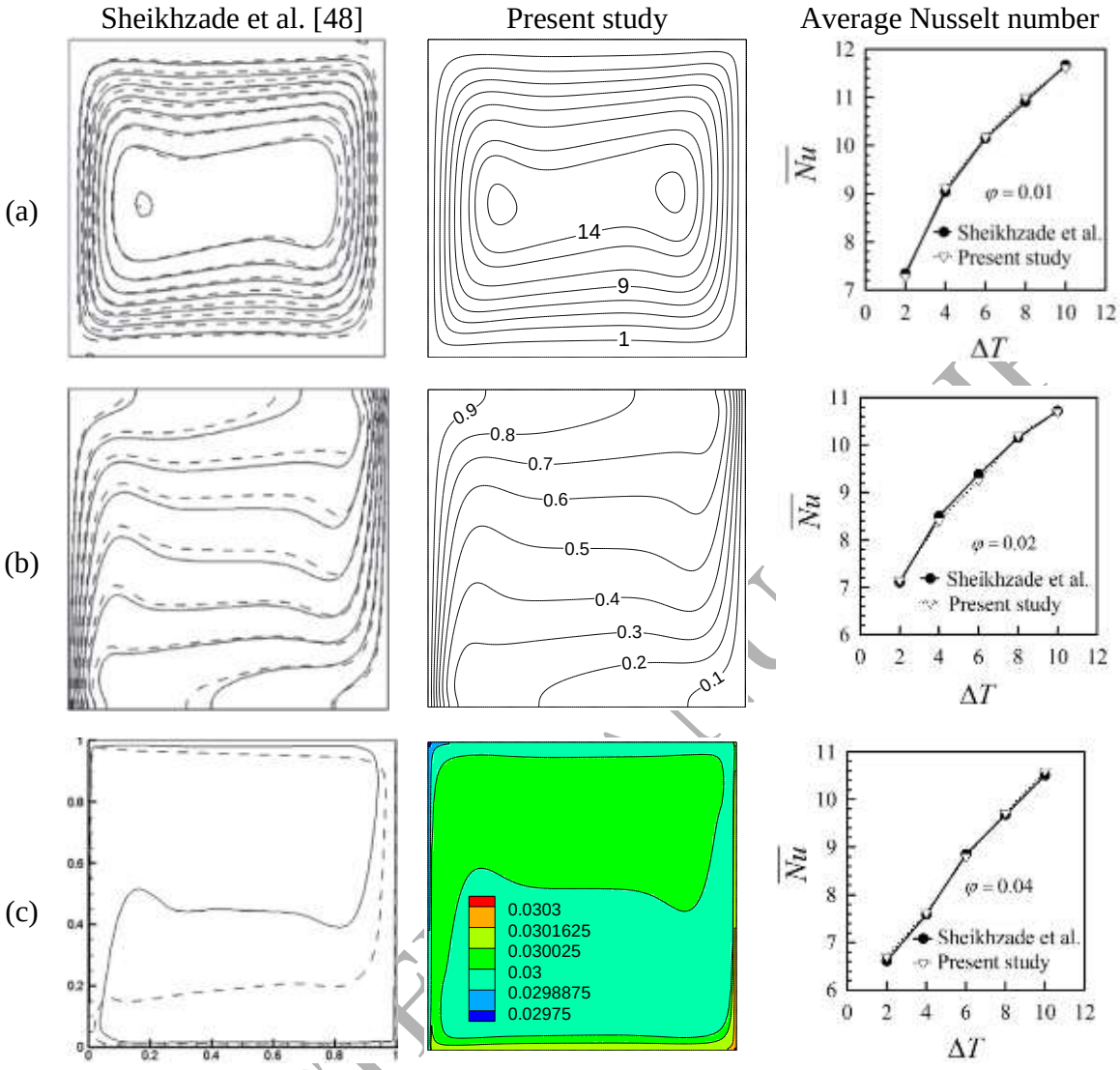

Fig. 3. Comparison of the (a) streamlines, (b) isotherms, averaged Nusselt number and (c) contours of nanoparticles distribution computed by Sheikhzadeh et al. [48] and computed with present code for various volume fractions of the nanoparticles.

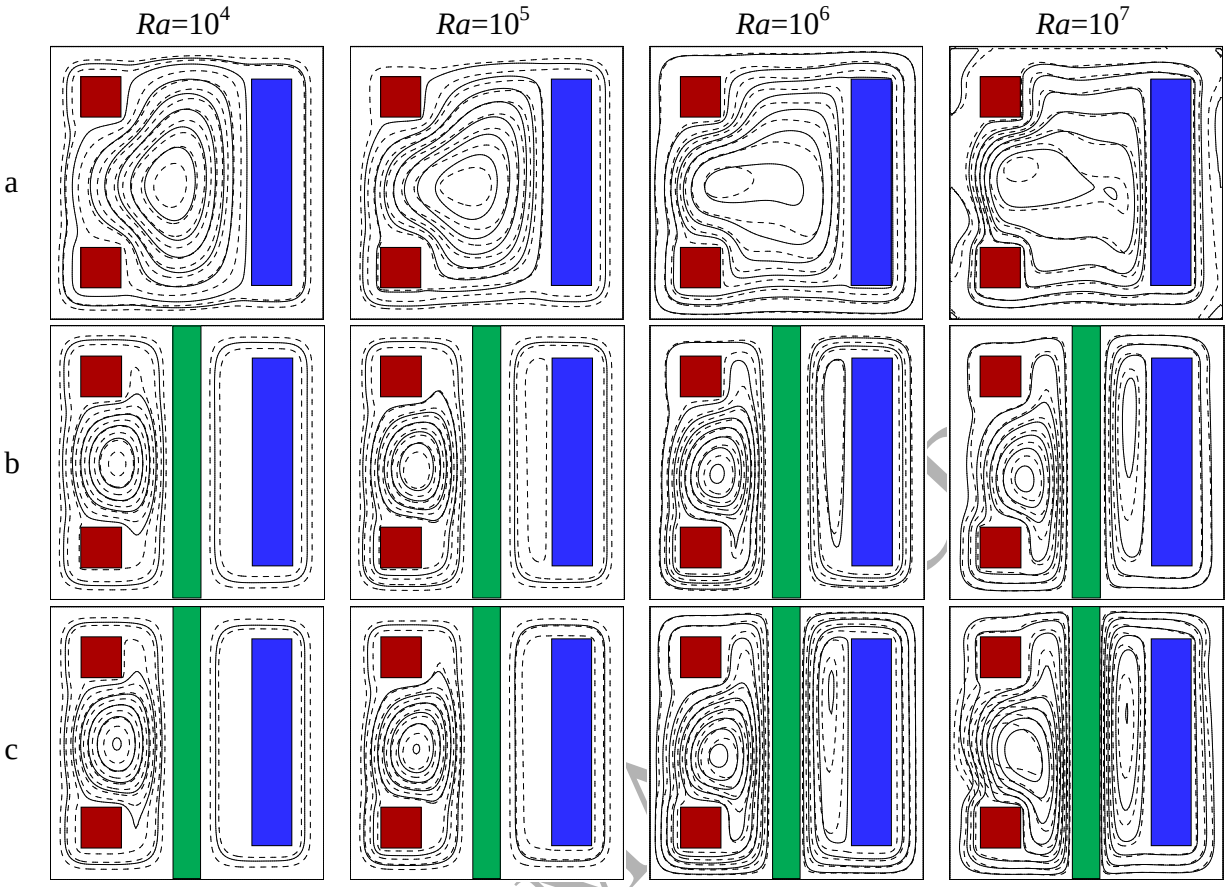

Fig. 4. Streamline inside the enclosure filled with the pure fluid (dashed lines) and TiO_2-water nanofluid (solid lines) with $\varphi = 0.05$ and $d_p = 25nm$ at different *Ra* for case 1A and 1B. (a) Case 1A, (b) Case 1B (K_r=0.2), (c) Case 1B (K_r=25). Heater (L_1=L_2=0.15*H*), cooler (L_1=0.75*H*, L_2=0.15*H*) and conductive partition (L_1=1.0*H*, L_2=0.1*H*).

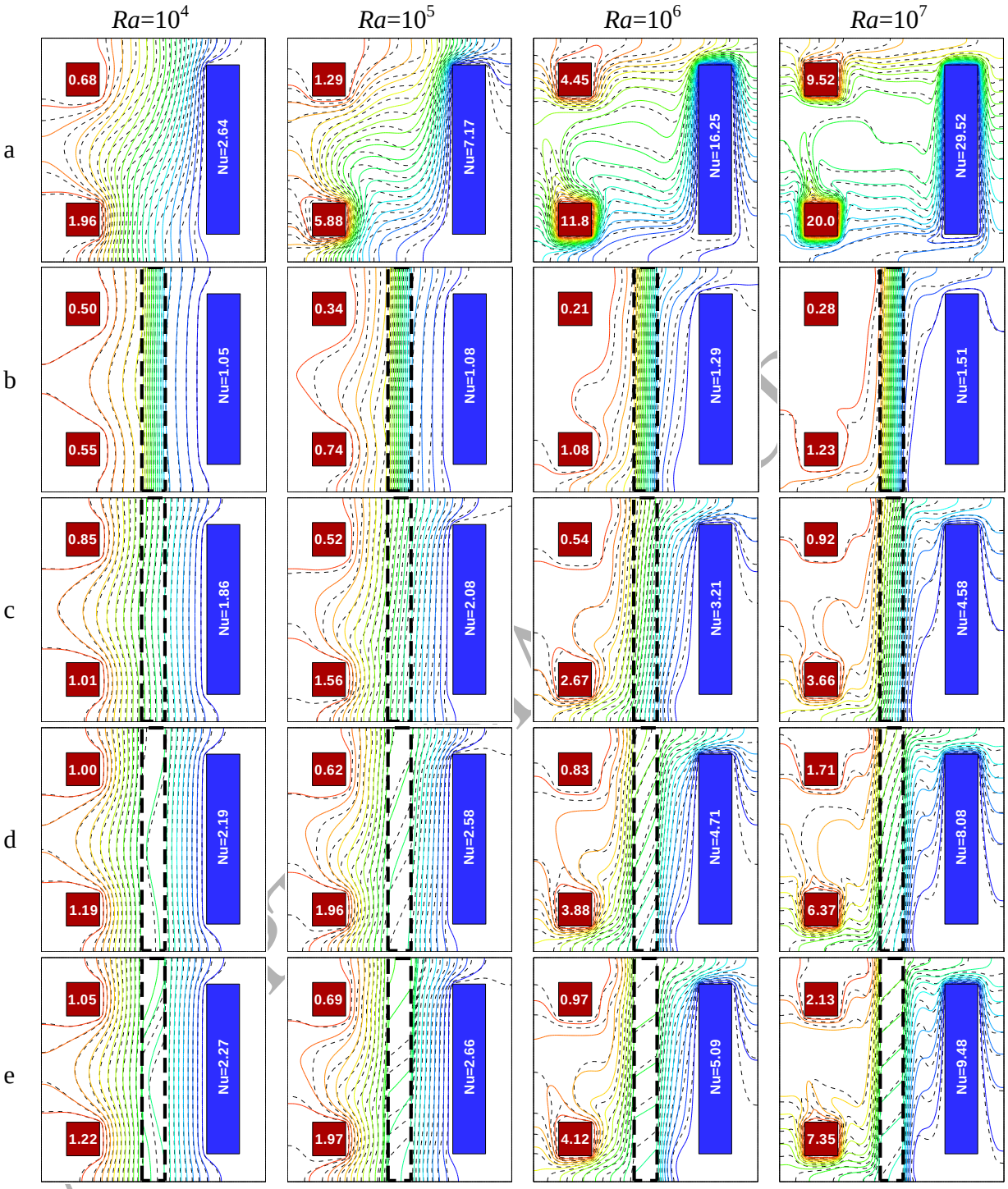

Fig. 5. Isotherm inside the enclosure filled with the pure fluid (dashed lines) and TiO_2-water nanofluid (solid lines) with $\varphi = 0.05$ and $d_p = 25nm$ at different *Ra* for case 1A and 1B. (a) Case 1A, (b) Case 1B (K_r=0.2), (c) Case 1B (K_r=1), (d) Case 1B (K_r=5) and (e) Case 1B (K_r=25). Heater (L_1=L_2=0.15H), cooler (L_1=0.75H, L_2=0.15H) and conductive partition (L_1=1.0H, L_2=0.1H).

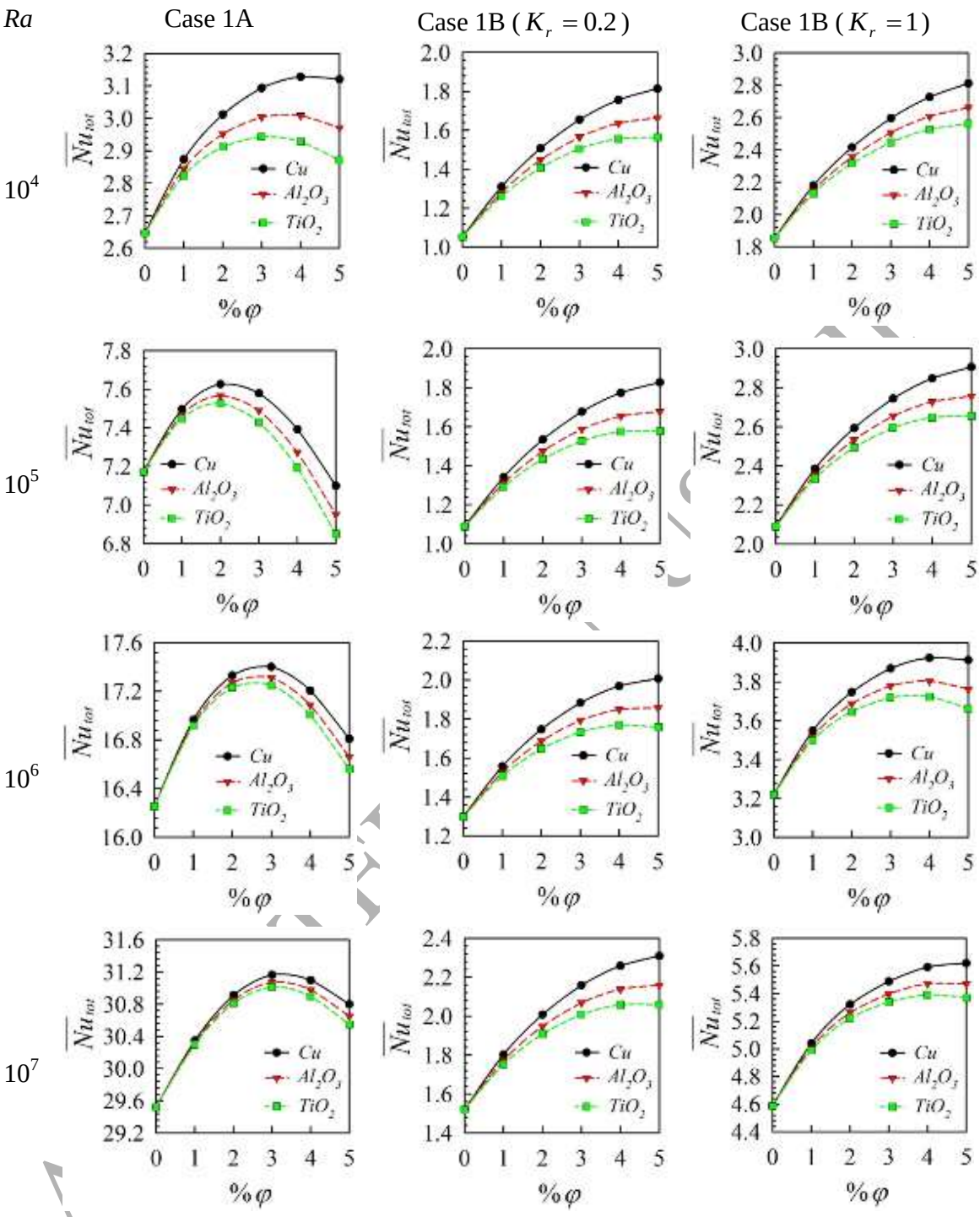

Fig. 6. Variations of the total Nusselt number with respect to volume fraction and type of the nanoparticles at different Rayleigh numbers for case 1A and 1B.

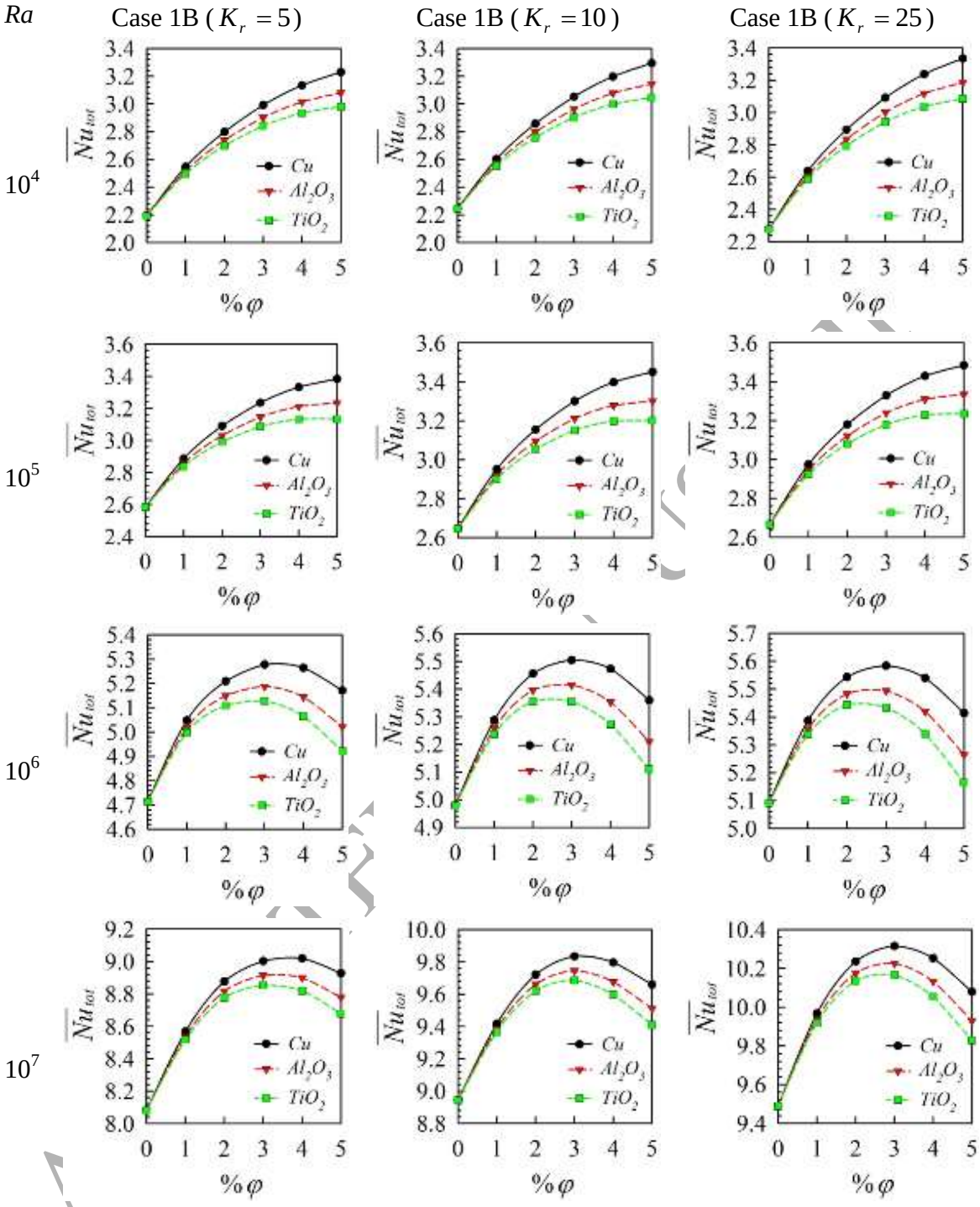

Fig. 6. (continued)

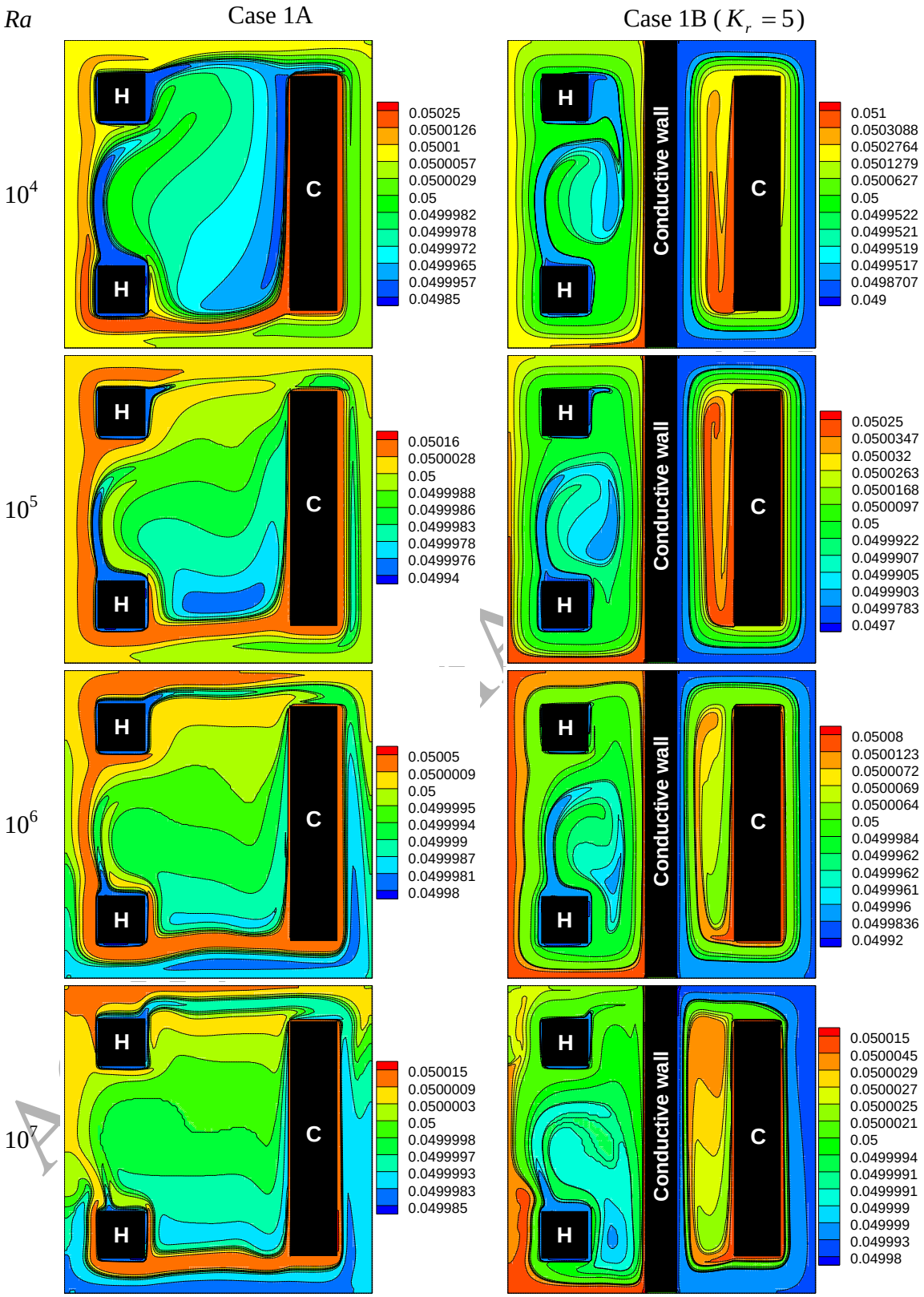

Fig. 7. Contours of the solid particles (*Cu*) distribution with $\varphi = 0.05$ and $d_p = 25nm$ at different *Ra*.

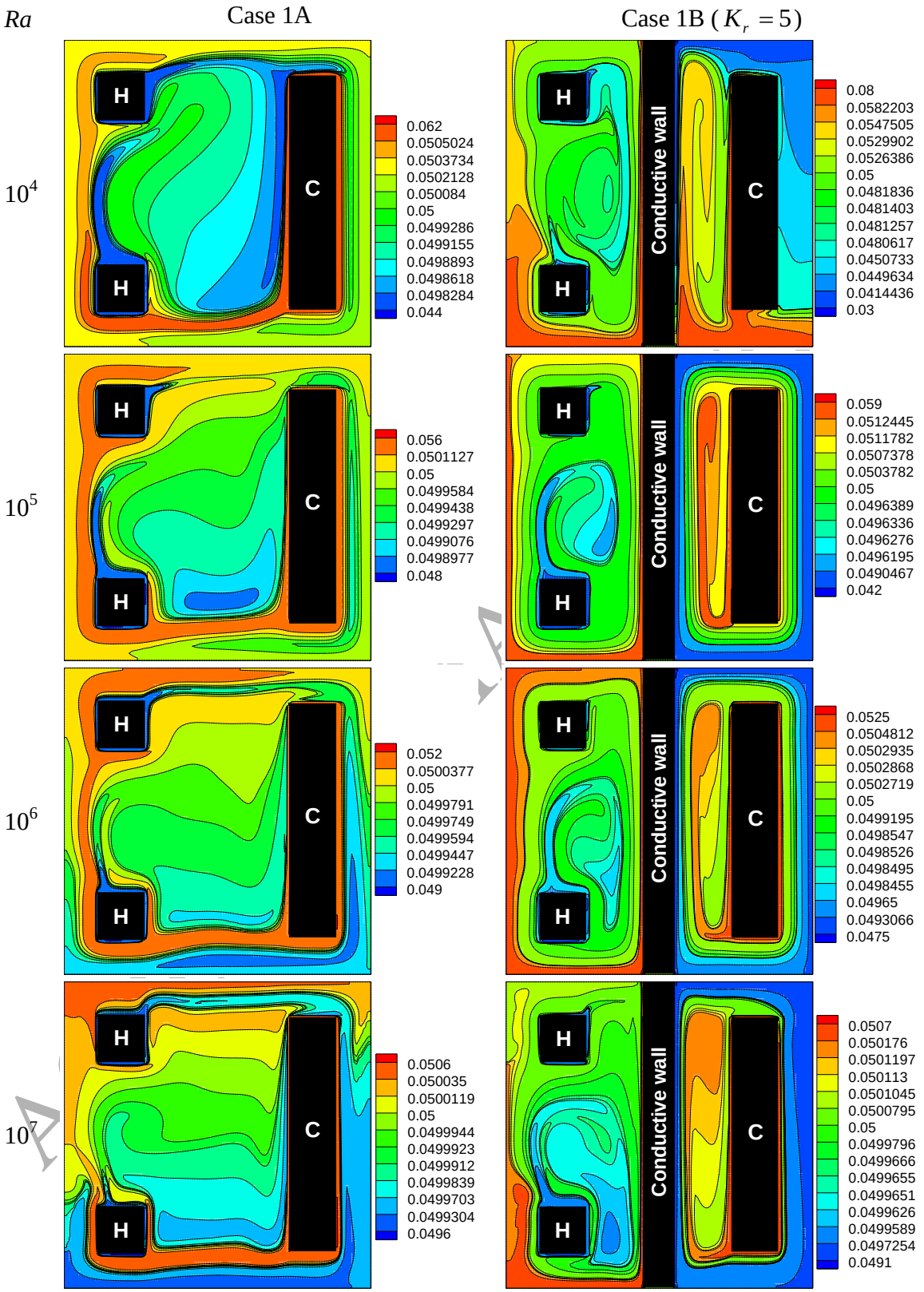

Fig. 8. Contours of the solid particles (TiO_2) distribution with $\varphi = 0.05$ and $d_p = 25nm$ at different *Ra*.

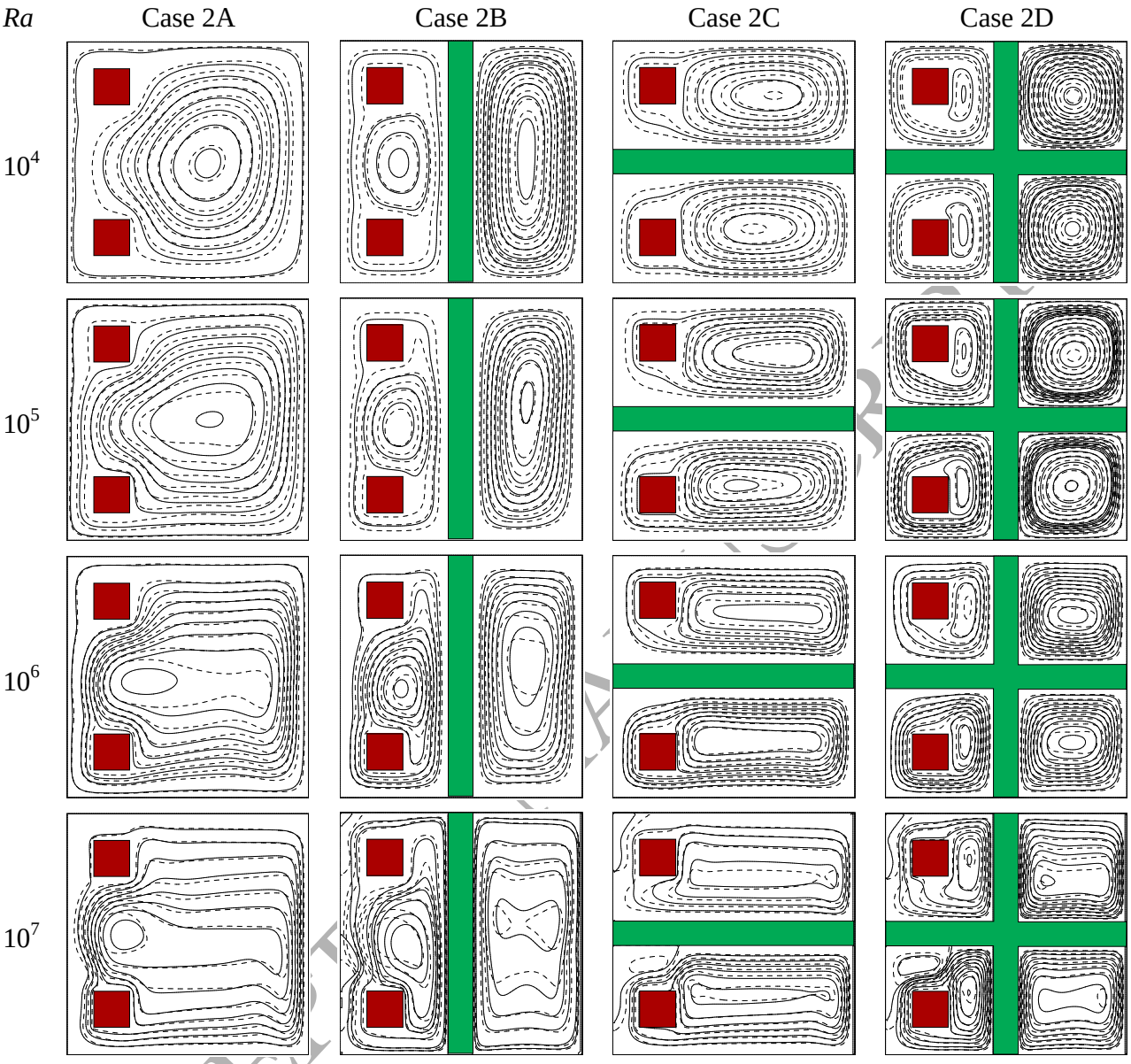

Fig. 9. Streamline inside the enclosure filled with the pure fluid (dashed lines) and Al_2O_3-water nanofluid (solid lines) with $\varphi = 0.05$ and $d_p = 25nm$ at different *Ra* for case 2A to 2D. K_r=10. Heater (L_1=L_2=0.15H), cold surface (W=0.3H), conductive partition: vertical (L_1=1.0H, L_2=0.1H) and horizontal (L_1=0.1H, L_2=1.0H).

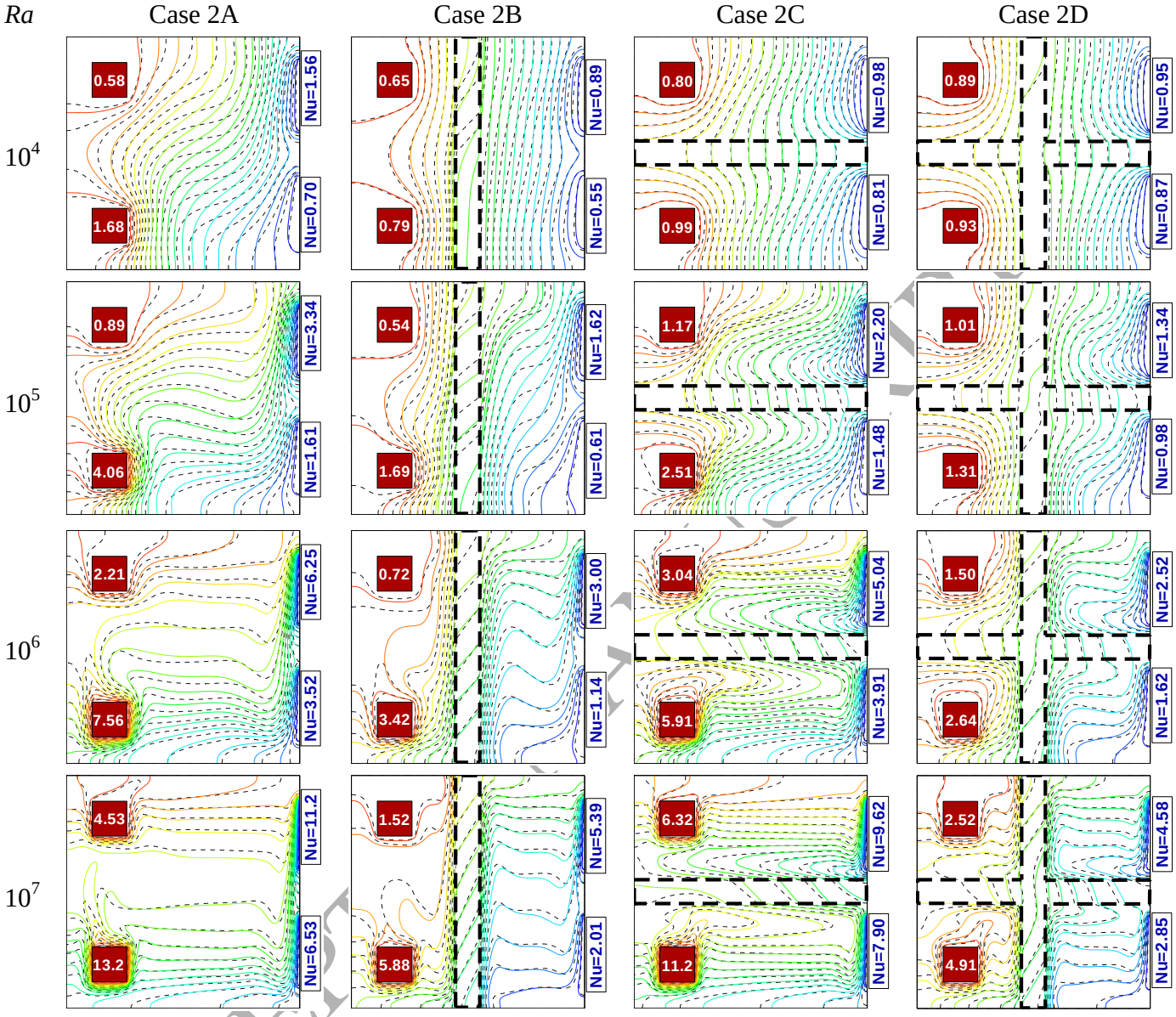

Fig. 10. Isotherm inside the enclosure filled with the pure fluid (dashed lines) and Al_2O_3-water nanofluid (solid lines) with $\varphi = 0.05$ and $d_p = 25nm$ at different *Ra* for case 2A to 2D. K_r=10. Heater (L_1=L_2=0.15H), cold surface (W=0.3H), conductive partition: vertical (L_1=1.0H, L_2=0.1H) and horizontal (L_1=0.1H, L_2=1.0H).

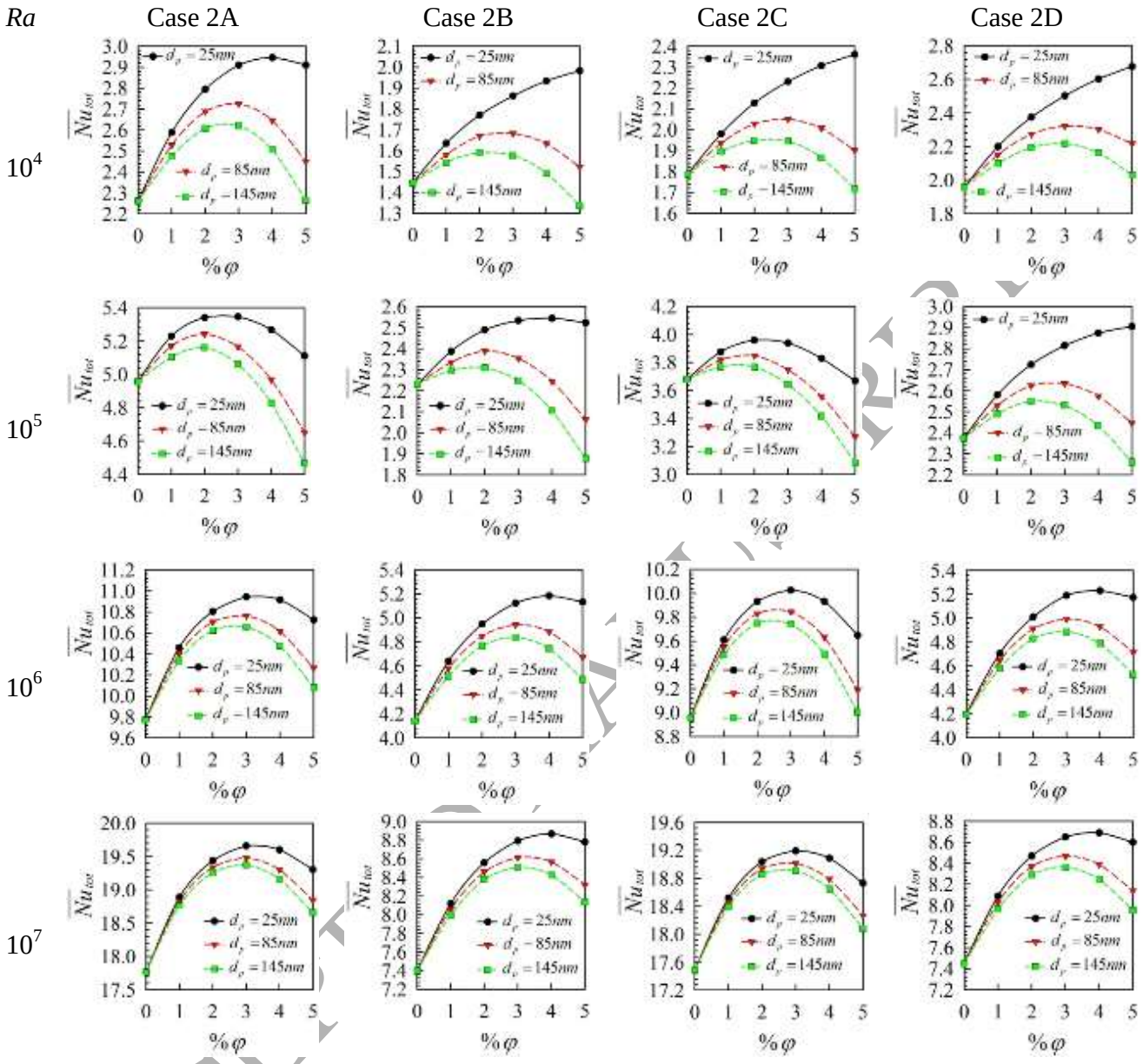

Fig. 11. Variations of the total Nusselt number with respect to volume fraction and diameter of the nanoparticles at different Rayleigh numbers for case 2A to 2D. K_r=10.

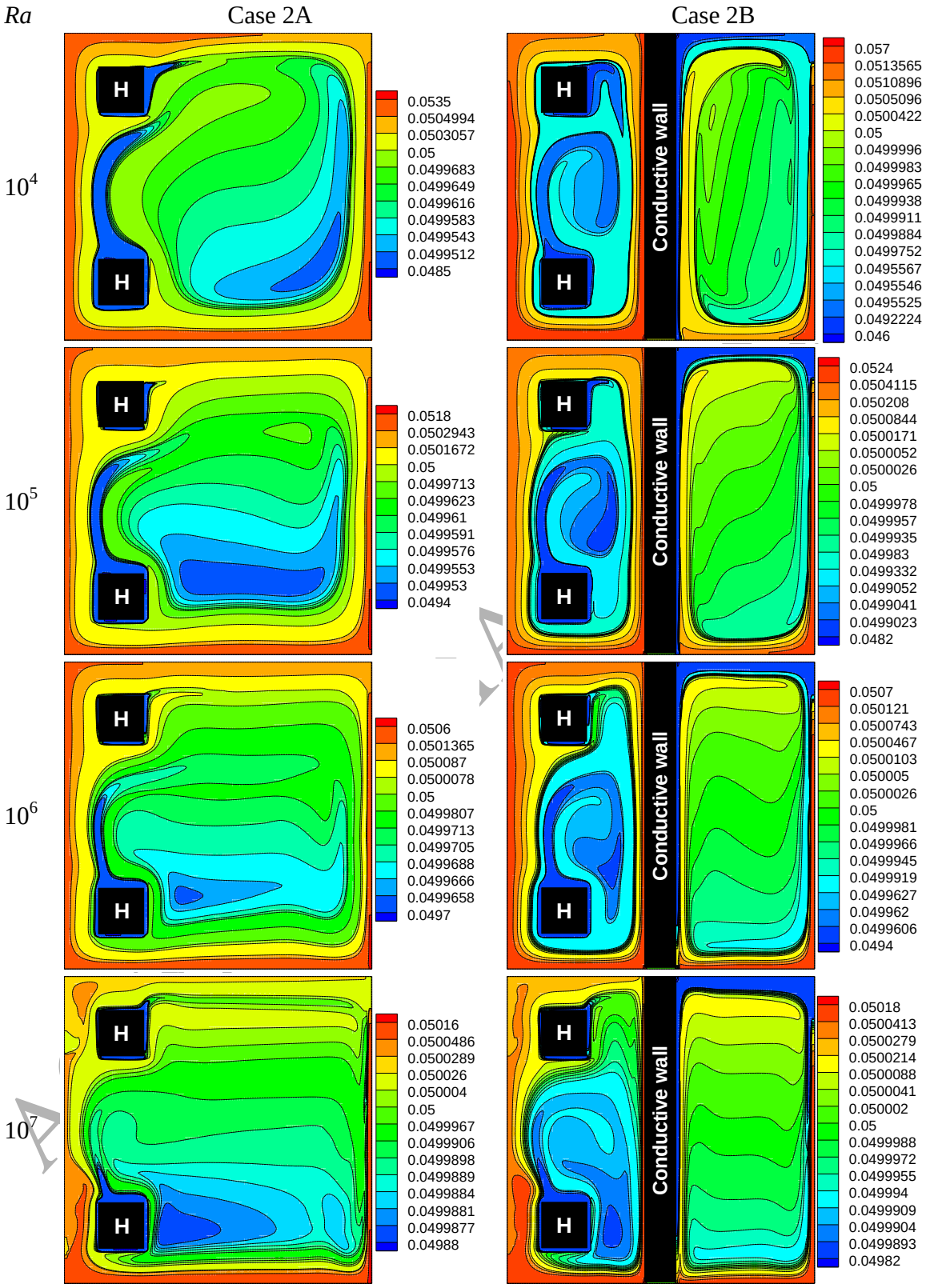

Fig. 12. Contours of solid particles (Al_2O_3) distribution with $\varphi = 0.05$ and $d_p = 25nm$ at different *Ra*.

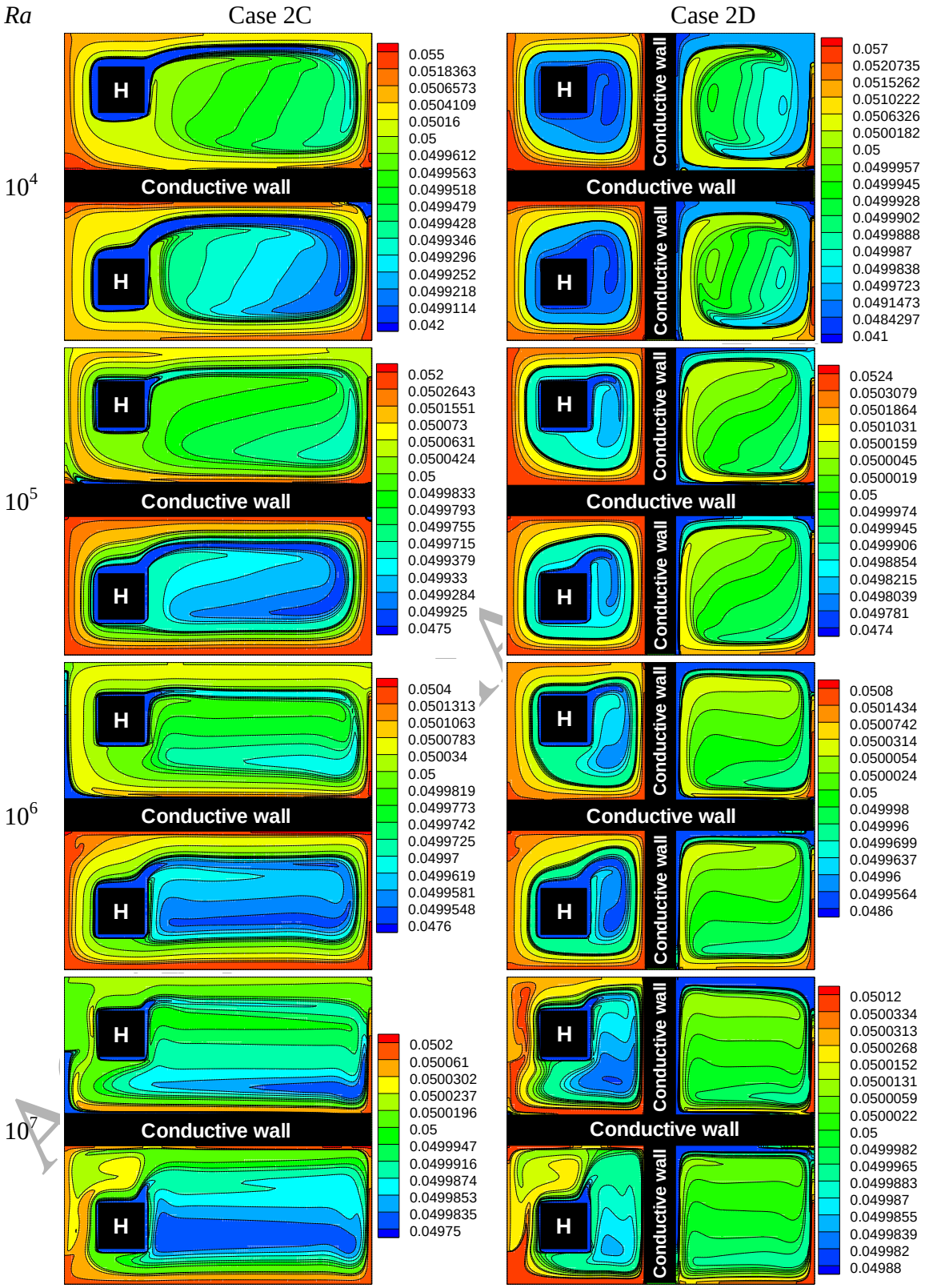

Fig. 12. (continued)

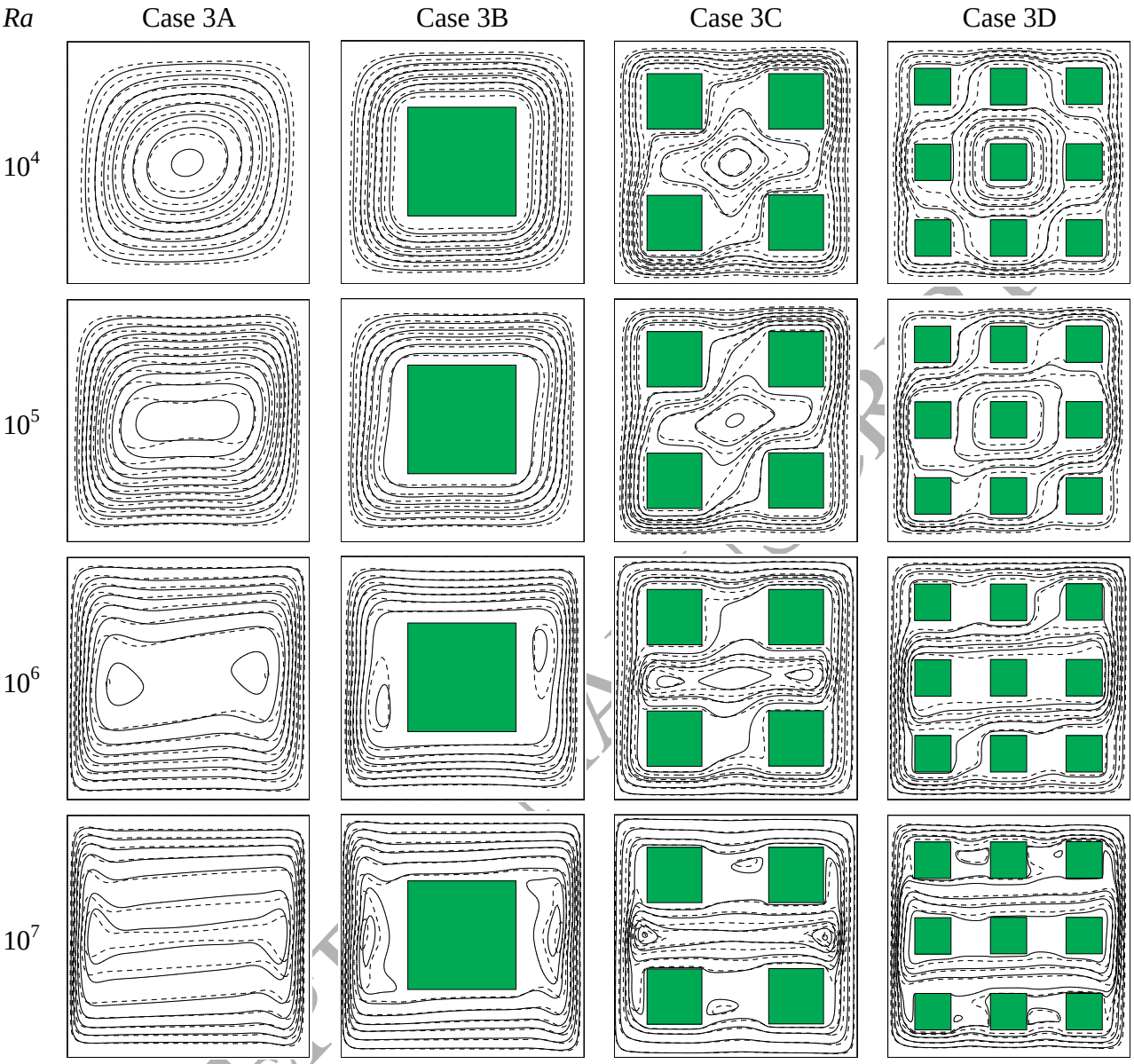

Fig. 13. Streamline inside the enclosure filled with the pure fluid (dashed lines) and Al_2O_3-water nanofluid (solid lines) with $\varphi = 0.05$ and $d_p = 25nm$ at different *Ra* for case 3A to 3D. K_r=0.1. Hot and cold surfaces (W=*0.35H*), conductive obstacle: case 3B (L_1=L_2=0.45*H*), case 3C (L_1=L_2=0.225*H*) and case 3D (L_1=L_2=0.15*H*).

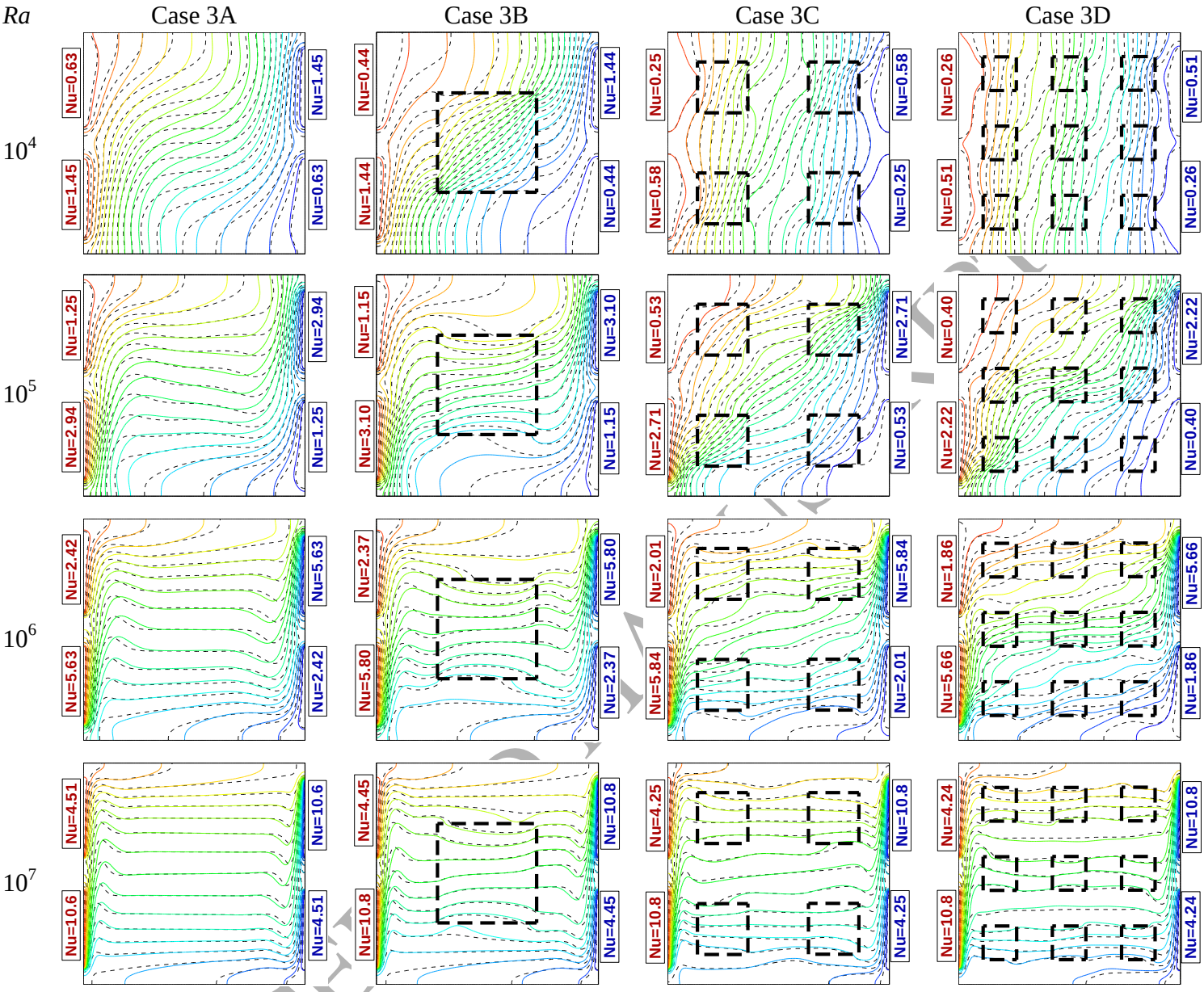

Fig. 14. Isotherm inside the enclosure filled with the pure fluid (dashed lines) and Al_2O_3-water nanofluid (solid lines) with $\varphi = 0.05$ and $d_p = 25nm$ at different *Ra* for case 3A to 3D. K_r=0.1. Hot and cold surfaces (W=0.35H), conductive obstacle: case 3B (L_1=L_2=0.45H), case 3C (L_1=L_2=0.225H) and case 3D (L_1=L_2=0.15H).

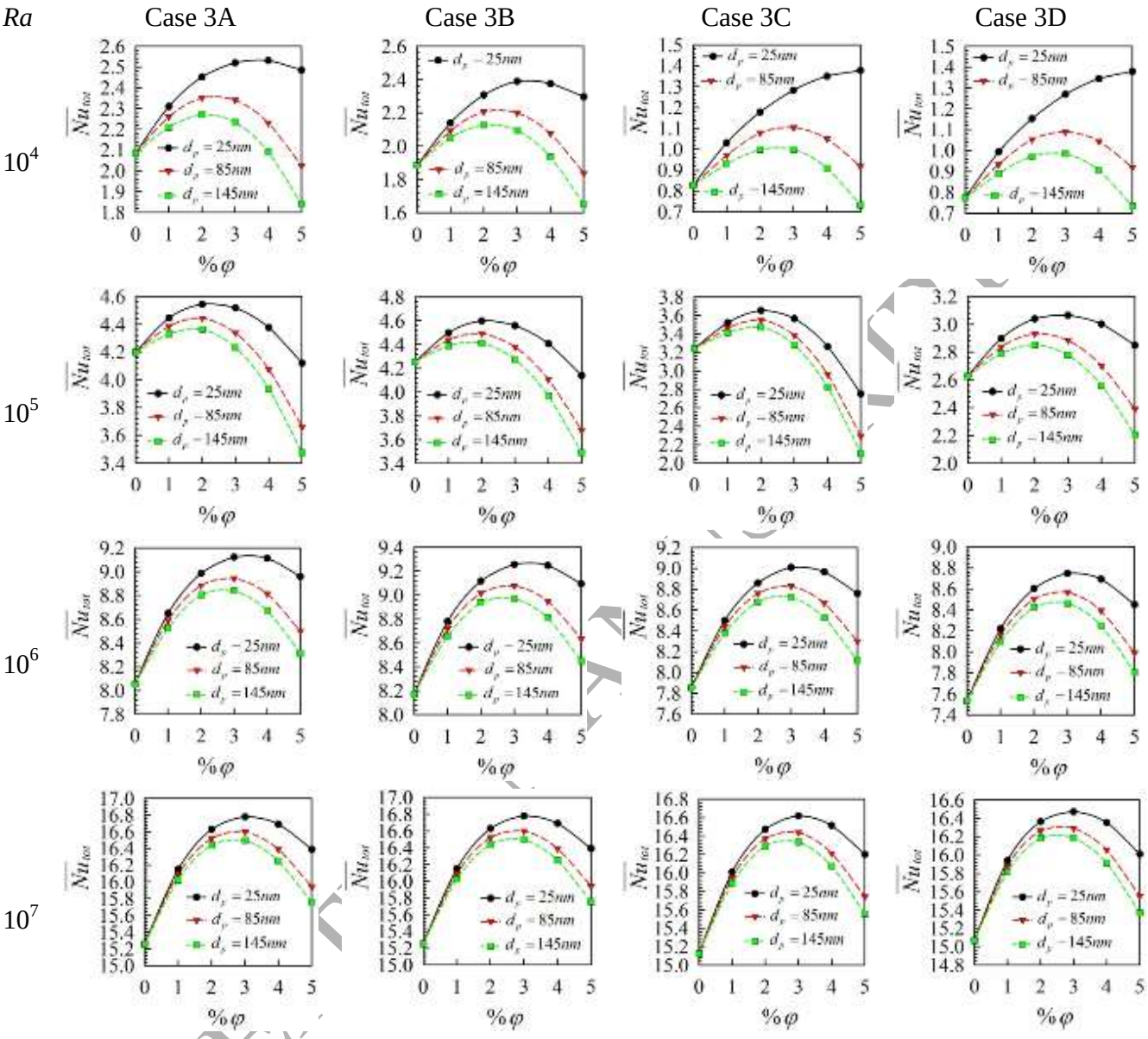

Fig. 15. Variations of the total Nusselt number with respect to volume fraction and diameter of the nanoparticles at different Rayleigh numbers for case 3A to 3D (K_r=10).

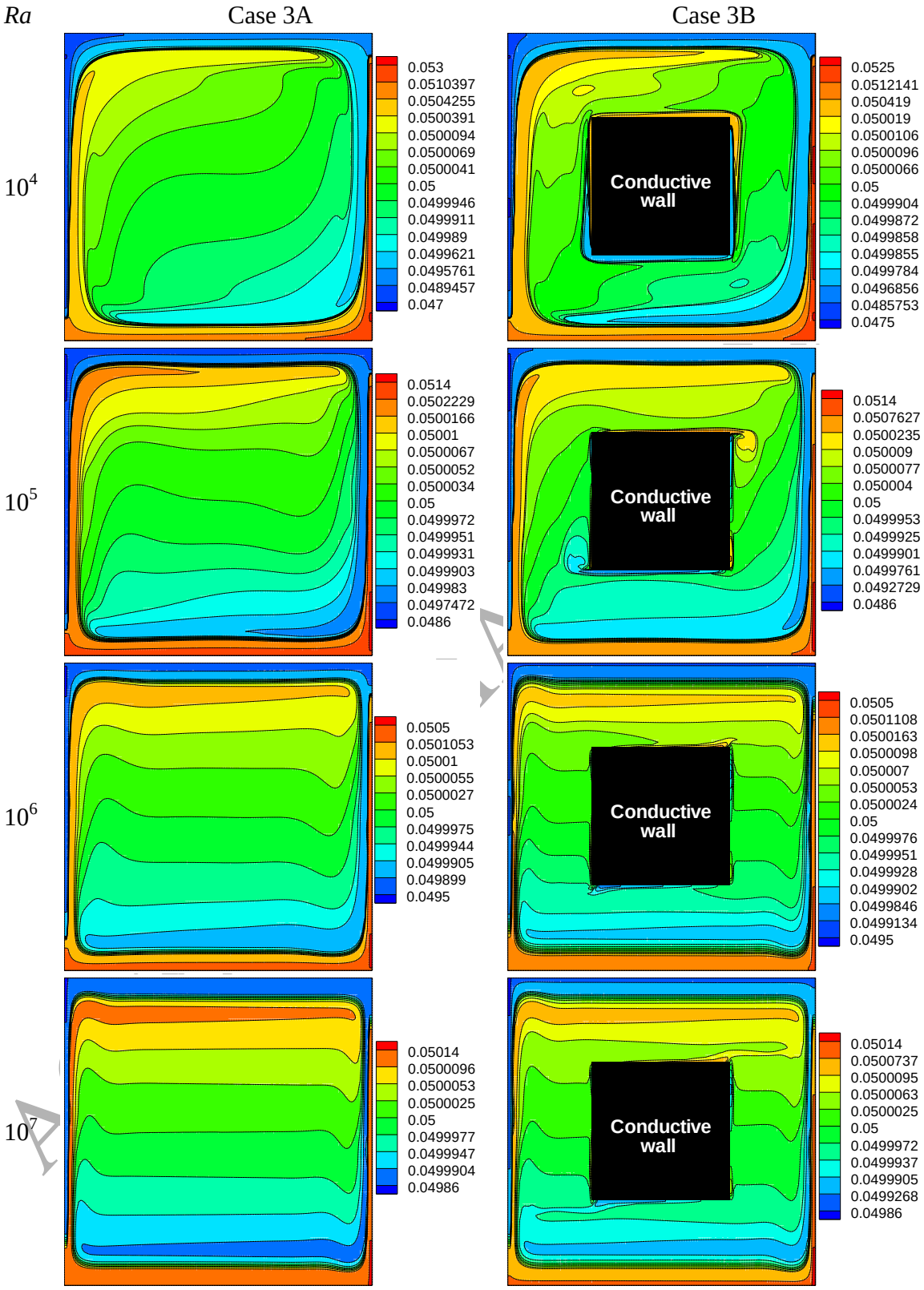

Fig. 16. Contours of solid particles (Al_2O_3) distribution with $\varphi = 0.05$ and $d_p = 25nm$ at different *Ra*.

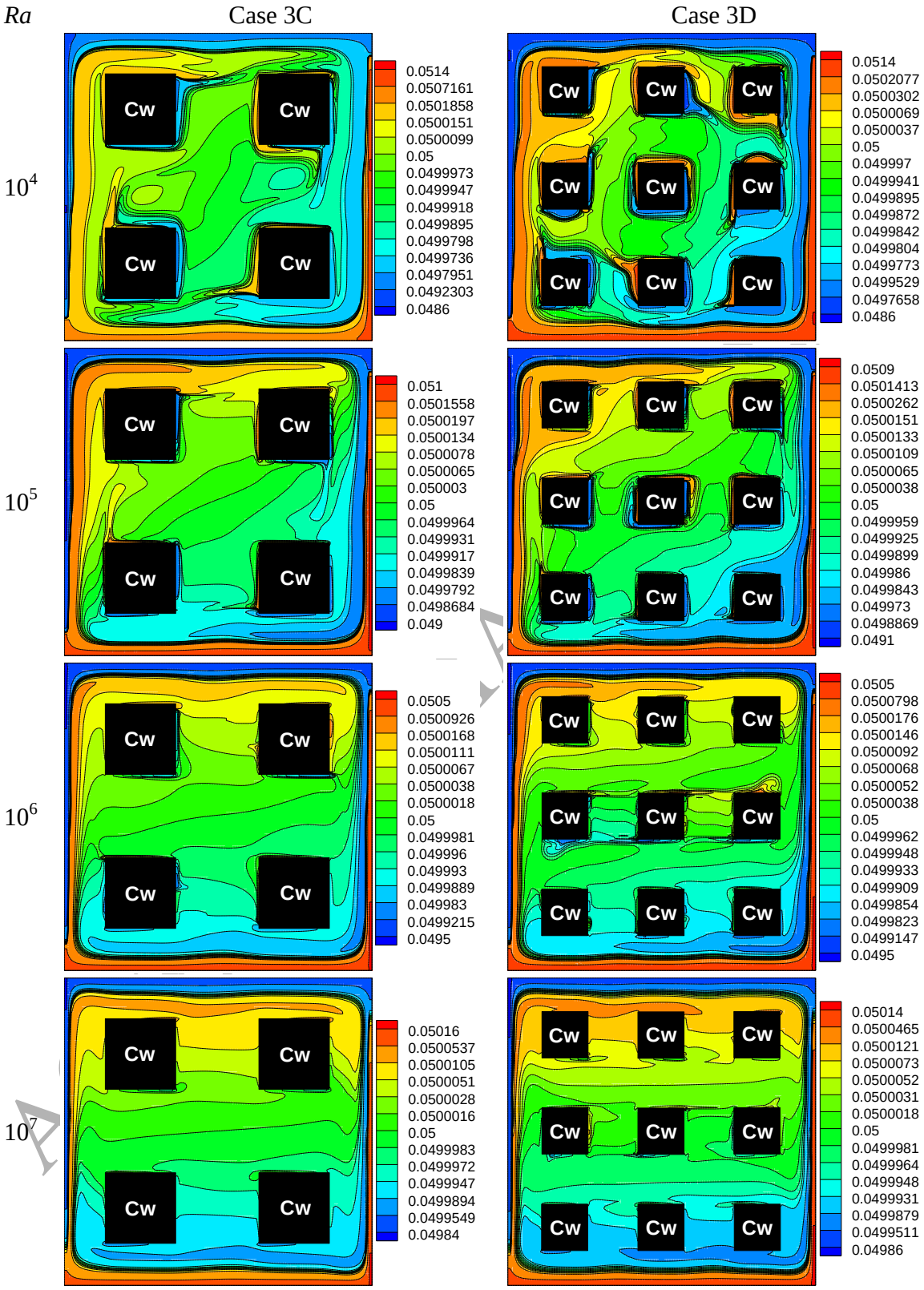

Fig. 16. (continued)

Table 1. Thermo-physical properties of water and nanoparticles at T=310 K [50]

Soild	$\rho(kg/m^3)$	$K(w/mK)$	$C_p(j/kgK)$	$\beta\times10^5(K^{-1})$	$\mu\times10^6(\mathrm{kg\,m^{-1}\,s^{-1}})$	$d_p(nm)$
Cu	8933	401	385	1.67	-----	25, 85, 145
Al_2O_3	3970	36	765	0.85	-----	25, 85, 145
TiO_2	4157	8.4	710	0.9	-----	25, 85, 145
*Wate*r	993	0.628	4178	36.2	695 (Pr=4.62)	0.385

Table 2. Effect of the grid size on $\overline{Nu}_{tot}$ for cases 1A, 2D and 3D. Square cavity filled with nanofluid ($\varphi_p = 0.05$, d_p=25).

Grid size (Case 1A) (TiO_2-water)							
Ra	49×49	69×69	89×89	109×109	129×129	149×149	169×169
10^4	2.8133	2.8408	2.8584	2.8657	2.8691	2.8702	2.8705
10^7	30.4826	30.5131	30.5317	30.5404	30.5461	30.5485	30.5489
Grid size (Case 2D) (Al_2O_3-water) (K_r=10)							
Ra	49×49	69×69	89×89	109×109	129×129	149×149	169×169
10^4	2.6118	2.6432	2.6584	2.6707	2.6751	2.6763	2.6769
10^7	8.5166	8.5519	8.5706	8.5827	8.5943	8.5992	8.5997
Grid size (Case 3D) (Al_2O_3-water) (K_r=10)							
Ra	49×49	69×69	89×89	109×109	129×129	149×149	169×169
10^4	1.3439	1.3558	1.3607	1.3685	1.3766	1.3791	1.3794
10^7	15.5016	15.7185	15.8602	15.9706	16.0044	16.0107	16.0113

Table. 3. Variations of $|\psi_{\max}|$ with respect to volume fraction of the nanoparticles and thermal conductivity of the vertical wall at different Rayleigh numbers for case 1A and 1B. d_p=25*nm*. TiO_2-water.

Ra	Case	$\varphi = 0$	$\varphi = \%1$	$\varphi = \%2$	$\varphi = \%3$	$\varphi = \%4$	$\varphi = \%5$
10^4	1A	3.59	3.43	3.19	2.92	2.62	2.30
	1B ($K_r = 0.2$)	0.35	0.32	0.29	0.25	0.22	0.19
	1B ($K_r = 1$)	0.60	0.55	0.49	0.44	0.38	0.33
	1B ($K_r = 5$)	0.69	0.63	0.57	0.50	0.44	0.37
	1B ($K_r = 10$)	0.70	0.64	0.58	0.51	0.45	0.38
	1B ($K_r = 25$)	0.71	0.65	0.58	0.51	0.45	0.38
Ra	Case	$\varphi = 0$	$\varphi = \%1$	$\varphi = \%2$	$\varphi = \%3$	$\varphi = \%4$	$\varphi = \%5$
10^5	1A	13.48	13.51	13.16	12.64	11.99	11.20
	1B ($K_r = 0.2$)	2.83	2.68	2.49	2.27	2.03	1.78
	1B ($K_r = 1$)	4.44	4.26	3.98	3.67	3.32	2.93
	1B ($K_r = 5$)	5.15	4.94	4.62	4.25	3.84	3.39
	1B ($K_r = 10$)	5.30	5.07	4.74	4.36	3.93	3.46
	1B ($K_r = 25$)	5.43	5.18	4.84	4.44	4.00	3.52
Ra	Case	$\varphi = 0$	$\varphi = \%1$	$\varphi = \%2$	$\varphi = \%3$	$\varphi = \%4$	$\varphi = \%5$
10^6	1A	36.57	36.84	36.14	35.05	33.66	31.95
	1B ($K_r = 0.2$)	10.93	10.95	10.66	10.25	9.72	9.07
	1B ($K_r = 1$)	15.64	15.70	15.32	14.78	14.09	13.22
	1B ($K_r = 5$)	18.12	18.19	17.76	17.12	16.30	15.30
	1B ($K_r = 10$)	18.80	18.86	18.41	17.74	16.89	15.85
	1B ($K_r = 25$)	19.73	19.77	19.28	18.55	17.64	16.52
Ra	Case	$\varphi = 0$	$\varphi = \%1$	$\varphi = \%2$	$\varphi = \%3$	$\varphi = \%4$	$\varphi = \%5$
10^7	1A	82.80	83.71	83.07	82.01	80.59	78.61
	1B ($K_r = 0.2$)	26.66	27.10	26.89	26.46	25.83	24.96
	1B ($K_r = 1$)	36.44	37.74	37.83	37.39	36.51	35.20
	1B ($K_r = 5$)	41.34	42.70	43.02	42.98	42.49	41.36
	1B ($K_r = 10$)	42.76	44.11	44.40	44.38	43.93	42.86
	1B ($K_r = 25$)	44.64	46.07	46.43	46.46	46.03	44.91

Table. 4. Variations of $|\psi_{\max}|$ with respect to volume fraction of the nanoparticles at different Rayleigh numbers for case 2A to 2D. d_p=25*nm*. Al_2O_3-water.

Ra	Case	$\varphi = 0$	$\varphi = \%1$	$\varphi = \%2$	$\varphi = \%3$	$\varphi = \%4$	$\varphi = \%5$
10^4	2A	4.67	4.62	4.44	4.21	3.92	3.58
	2B (K_r=10)	1.31	1.21	1.10	0.99	0.87	0.75
	2C (K_r=10)	1.01	0.94	0.85	0.76	0.67	0.57
	2D (K_r=10)	0.66	0.61	0.55	0.49	0.43	0.36
Ra	Case	$\varphi = 0$	$\varphi = \%1$	$\varphi = \%2$	$\varphi = \%3$	$\varphi = \%4$	$\varphi = \%5$
10^5	2A	11.83	12.08	12.00	11.80	11.49	11.07
	2B (K_r=10)	6.18	6.14	5.93	5.65	5.30	4.89
	2C (K_r=10)	5.28	5.18	4.95	4.67	4.34	3.96
	2D (K_r=10)	3.88	3.81	3.65	3.44	3.18	2.89
Ra	Case	$\varphi = 0$	$\varphi = \%1$	$\varphi = \%2$	$\varphi = \%3$	$\varphi = \%4$	$\varphi = \%5$
10^6	2A	28.31	28.82	28.51	27.91	27.07	25.98
	2B (K_r=10)	17.29	17.36	16.96	16.35	15.57	14.61
	2C (K_r=10)	15.51	15.78	15.57	15.17	14.61	13.89
	2D (K_r=10)	9.44	9.78	9.84	9.79	9.63	9.36
Ra	Case	$\varphi = 0$	$\varphi = \%1$	$\varphi = \%2$	$\varphi = \%3$	$\varphi = \%4$	$\varphi = \%5$
10^7	2A	61.39	62.42	61.97	61.04	59.74	58.08
	2B (K_r=10)	39.54	40.86	41.17	41.07	40.48	39.26
	2C (K_r=10)	30.18	31.26	31.43	31.32	30.98	30.44
	2D (K_r=10)	21.45	21.92	21.77	21.38	20.80	20.03

Table. 5. Variations of $|\psi_{\max}|$ with respect to volume fraction of the nanoparticles at different Rayleigh numbers for case 3A to 3D. d_p=25*nm*. Al_2O_3-water.

Ra	Case	$\varphi = 0$	$\varphi = \%1$	$\varphi = \%2$	$\varphi = \%3$	$\varphi = \%4$	$\varphi = \%5$
10^4	3A	4.97	4.92	4.85	4.66	4.40	4.08
	3B(K_r=10)	2.37	2.31	2.19	2.04	1.87	1.68
	3C(K_r=10)	0.88	0.80	0.73	0.64	0.56	0.48
	3D (K_r=10)	0.72	0.67	0.61	0.54	0.48	0.41
Ra	Case	$\varphi = 0$	$\varphi = \%1$	$\varphi = \%2$	$\varphi = \%3$	$\varphi = \%4$	$\varphi = \%5$
10^5	3A	10.60	10.93	10.94	10.85	10.68	10.43
	3B(K_r=10)	7.58	7.66	7.52	7.29	6.98	6.60
	3C(K_r=10)	5.53	5.43	5.19	4.87	4.49	4.04
	3D (K_r=10)	4.10	3.99	3.78	3.53	3.24	2.92
Ra	Case	$\varphi = 0$	$\varphi = \%1$	$\varphi = \%2$	$\varphi = \%3$	$\varphi = \%4$	$\varphi = \%5$
10^6	3A	19.01	19.82	20.02	20.03	19.89	19.60
	3B(K_r=10)	16.52	17.09	17.14	17.01	16.72	16.27
	3C(K_r=10)	15.00	15.18	14.91	14.48	13.90	13.35
	3D (K_r=10)	14.01	14.03	13.67	13.15	12.51	11.72
Ra	Case	$\varphi = 0$	$\varphi = \%1$	$\varphi = \%2$	$\varphi = \%3$	$\varphi = \%4$	$\varphi = \%5$
10^7	3A	34.03	35.26	35.49	35.35	34.98	34.33
	3B(K_r=10)	30.62	31.76	31.94	31.82	31.45	30.85
	3C(K_r=10)	33.42	34.34	34.30	33.91	33.24	32.25
	3D (K_r=10)	32.78	33.69	33.68	33.37	32.76	31.79

Graphical abstract